Joint Polarimetric Subspace Detector Based on Modified Linear Discriminant Analysis

Tao Liu, Ziyuan Yang, Armando Marino, *Member*, *IEEE*, Gui Gao, *Member*, *IEEE,* and Jian Yang, *Member*, *IEEE*

***Abstract*—Polarimetric synthetic aperture radar (PolSAR) is widely used in remote sensing and has important applications in the detection of ships. Although many polarimetric detectors have been proposed, they are not well combined. Recently, a polarimetric detection optimization filter (PDOF) was proposed that performs well in most environments. In this study, a novel subspace form of the PDOF (SPDOF) was further developed based on the Cauchy inequality and matrix decomposition theories, enhancing detection performance. Furthermore, a simple method to determine the optimal dimension of the subspace detector based on the trace ratio form was proposed by calculating the area under the receiver operating characteristic (ROC) curve, reaching the best detection performance among the subspaces of the detector. Moreover, to combine different subspace detectors, a modified linear discriminant analysis was proposed and developed to the diagonal loading detector (DLD) based on polarimetric subspaces. The experimental results demonstrate the superiority of these joint polarimetric subspace detectors. Most importantly, DLD solves for previous limitations due to the complex clutter background and achieves a performance comparable to that of the Wishart (Gaussian) distribution, particularly in the low target clutter ratio (TCR) case.**

***Index Terms*—Polarimetric synthetic aperture radar (PolSAR), Polarimetric detection, Subspace detection, Ship detection, Polarimetric detection optimization filter, Linear Discriminant Analysis, Diagonal loading**

I. INTRODUCTION

SYNTHETIC aperture radar (SAR) is widely used in ship detection. The intensity of the SAR image can be utilized to statistically test the backscattering of pixels, and an adaptive threshold can be set to maintain a constant probability of false alarm (PFA) (i.e., the constant false alarm rate (CFAR)) [1, 2]. The current challenges in ship detection mostly lie in two aspects: the first is to detect small ships densely packed in inshore regions while the second is to detect ships during the medium or high sea states. Particularly, small ship detection in complicated clutter backgrounds remains an ongoing problem. In this paper we focus on the small ship detection in complicated backgrounds. Polarization is an important property of electromagnetic waves. Polarimetric SAR (PolSAR) takes advantage of the polarization information to acquire more complete pictures of backscattering from targets, which has beneficial applications in target detection [1-4]. There are five main categories of PolSAR ship detectors: (1) independent polarization channel composition [5], (2) polarization optimization techniques [6], (3) polarimetric scattering mechanism [7], (4) ship wake detection [8], and (5) data-driven or machine learning [9]. In this study, we focus on the optimization method because it is effective and has a straightforward practical interpretation.

Optimal polarimetric detection (OPD) is based on the likelihood ratio test and theoretically provides the best detection performance under the assumption that targets and clutter are both Wishart distributed [10]. The optimal polarimetric contrast enhancement (OPCE) method, which is mathematically equivalent to the polarimetric matched filter (PMF), maximizes the target-to-clutter ratio (TCR) using optimal antenna polarization states [11, 12]. A generalized OPCE (GOPCE) was proposed to include different scattering mechanisms between targets and clutter [13]. Recently, a novel polarimetric contrast enhancement method based on the minimal clutter-to-signal ratio (MCSR) subspace was proven to be more flexible [14], where OPCE and GOPCE can be seen as special cases of MCSR. However, the optimal dimension of the MSCR subspace has yet to be resolved, and the solution for the optimization is only numerical. Touzi *et al*. devised a method to optimize the degree of polarization for enhanced ship detection, obtaining good results [15, 16]. Because speckle fluctuation critically influences the detection performance, the polarimetric whitening filter (PWF) was proposed for ship detection [17], which minimizes speckle fluctuation (or the standard deviation-to-mean ratio). The PWF detector was found to achieve a performance comparable to that of the OPD when the target statistics are not provided. Recently, a polarimetric notch filter (PNF) was proposed based on the physical behavior of sea clutter, which minimizes clutter power [18]. A statistical test on the PNF was conducted with some assumptions, and it exhibited excellent performance [6].

As noted by Novak *et al*., detection performance is not only dependent on TCR, but also depends on clutter fluctuation [19]. Combining the objectives of PMF and PWF, and inspired by the subspace theory of MCSR [14], Tao *et al*. proposed a

---

This work was supported in part by the National Natural Science Foundation of China under Project 62171452, 41822105, in part by Fundamental Research Funds for the Central Universities under Projects 2682020ZT34 and 2682021CX071, and in part by the State Key Laboratory of Geo-Information Engineering under Projects SKLGIE2020-Z-3-1 and SKLGIE2020-M-4-1.

T. Liu and Z. Yang are with the school of electronic engineering, Naval University of Engineering, Wuhan, 430033, China (e-mail: liutao1018@hotmail.com).

A. Marino is with the Faculty of Natural Sciences, University of Stirling, UK (armando.marino@stir.ac.uk).

G. Gao is with the Faculty of Geoscience and Environmental Engineering, Southwest Jiaotong University, Chengdu, 611756, China (e-mail: dellar@126.com).

J. Yang is with the department of electronic engineering, Tsinghua University, Beijing, 100084, China (e-mail:yangjian_ee@tsinghua.edu.cn).

polarimetric detection optimization filter (PDOF) and its approximate subspace form (APDOF), which can provide performance similar to those of the best traditional detectors [6]. However, the derivation of APDOF maximizes the numerator TCR and minimizes the denominator fluctuation independently [6], rather than maximizing the overall value of their ratios simultaneously, which is not a strict solution in mathematics. This results in APDOF representing the middle ground between the PMF and PWF, rather than combining the benefits of PWF and PMF. Determining the optimal subspace dimension for ship detection is another difficult task that remains to be solved.

It is well known that there are many polarimetric detectors at present. Each detector can be seen as extracting a feature that helps separate ships and clutter. The combination of outputs from different detectors remains an open problem, wherein linear discriminant analysis (LDA) is a good candidate for combining different features [20]. Yin *et al*. modified the GOPCE to improve the detection performance by considering both the signal clutter ratio and the clutter fluctuation; however, they did not provide a comparison against LDA [21]. In this study, we modified the LDA algorithm to a novel form, extending for the combination of different polarimetric detectors.

This paper proposes a joint polarimetric subspace detector based on a modified LDA (MLDA) and extend it to a diagonal loading detector (DLD). The main contributions of this study are as follows:

(1) A strict PDOF (SPDOF) subspace detector was proposed by maximizing the TCR over speckle variation. The full-dimensional PDOF was found to represent a special case of subspace detectors. The statistics of the SPDOF were derived in a Wishart distribution hypothesis based on the quadratic form.

(2) A method to determine the optimal dimension of the polarimetric subspace was proposed based on the statistics of the detection variable and the area under the curve (AUC) of the ROC curve. The algorithm chooses the dimension for the practicable optimal subspace detector.

(3) A joint polarimetric subspace detector was proposed to fuse all interesting polarimetric features based on the MLDA. Performance comparisons were made among all the mentioned polarimetric detectors.

(4) A novel trace-based polarimetric detector (diagonal loading detector, DLD) based on the composition of polarimetric subspaces was proposed for ship detection. It was found to significantly improve performance by choosing a suitable balance parameter. The experimental results showed that it can overcome the negative impact of complex clutter.

The remainder of this paper is organized as follows. Section II describes the traditional trace ratio detectors (MCSR detector *et al.*), including their subspace forms, and the strict form of the PDOF subspace (SPDOF) is derived based on the Cauchy inequality and matrix decomposition theories. The MLDA algorithm was proposed to combine different polarimetric features for detection. The DLD is proposed by combining the SPDOF and APDOF. Section III analyzes and validates all polarimetric detection methods and their comparisons using simulated data. The measured data were used to assess different polarimetric detectors in Section IV. Finally, Section V concludes the paper.

II. SUBSPACE DETECTORS AND THEIR COMBINATION

This section summarizes and improves the previous subspace detectors and provides a method for their combinations. Firstly, we summarize the expression forms of the polarimetric detectors based on polarization techniques to be the trace ratio problem. We analyze and compare both the trace ratio and ratio trace forms and explain the relationship between them. Secondly, the APDOF is improved to the SPDOF, which is a strict subspace form of PDOF. PDOF performs better in complicated clutter background compared with the OPD. Thirdly, the statistics of the subspace detectors are presented, which helps to derive the optimal subspace dimension. Finally, MLDA method is used to combine the above different polarimetric detectors, and a DLD detector is proposed by further optimization, which is the best detector compared with all the state-of-art methods. The structures of parts A, B, C, D, and E and their relationships are shown in Figure 1. The workflow is indicated by the solid arrow lines. The rectangular boxes within the gray background regions show the operation and procedure. ≈ means trace ratio solution can be approximated by the ratio trace solution.

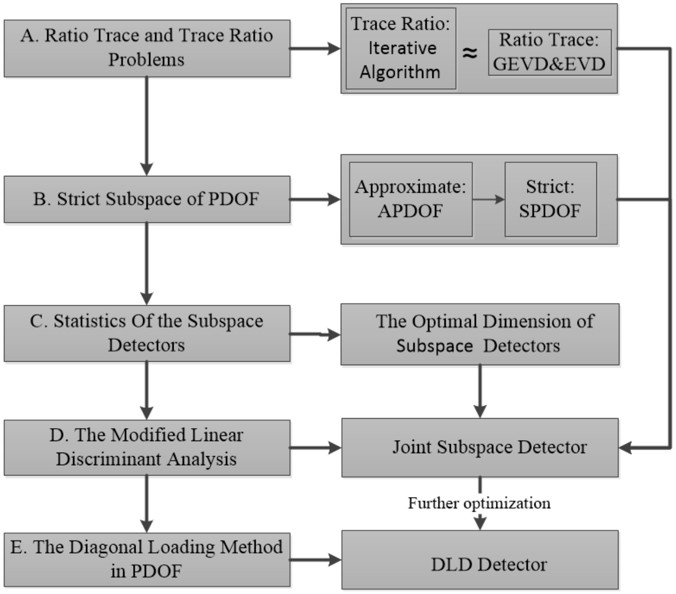

Fig. 1. Structure of Section II

A. Trace Ratio and Ratio Trace Problems

MCSR is defined to maximize the TCR [22] and is a typical trace ratio problem [23]. Meanwhile we can consider that some polarimetric detectors based on optimization techniques, such as OPD and PWF, can also be interpreted as a trace ratio problem [6]. The TCR is defined in (1):

$$TCR = \frac{\text{tr}(\mathbf{P}\mathbf{\Sigma}_T)}{\text{tr}(\mathbf{P}\mathbf{\Sigma}_C)} \tag{1}$$

where TCR is the m-dimensional MCSR, $\text{tr}(\bullet)$ is the trace operator, $(\bullet)^H$ denotes the conjugate transpose, and $\mathbf{\Sigma}_T$ and $\mathbf{\Sigma}_C$ are the positive semi-definite polarimetric covariance matrices of a target and clutter, respectively. The dimensions of the polarimetric matrix are n, the projection subspace dimension is m, and generally $m \le n$. The size of $\mathbf{F}$ is $n \times m$. The matrix $\mathbf{F}$ satisfies $\mathbf{F}^H\mathbf{F} = \mathbf{I}$, which denotes the matrix of the projected basis vectors. $\mathbf{I}$ denotes the identity matrix. Here, $\mathbf{P} = \mathbf{F}\mathbf{F}^H$ is an orthogonal projection matrix and also a positive semi-definite Hermitian matrix. [6].

Because the trace ratio problem does not have a closed-form solution, it is often simplified as a ratio trace problem, which is equivalent to the determinant ratio problem [23]:

$$\begin{aligned} r_{\max} &= \max_{\dim(\mathbf{F}^H\mathbf{F})=m} \operatorname{tr}\left[(\mathbf{F}^H\boldsymbol{\Sigma}_C\mathbf{F})^{-1}(\mathbf{F}^H\boldsymbol{\Sigma}_T\mathbf{F})\right] \\ &= \max_{\dim(\mathbf{F}^H\mathbf{F})=m} \frac{\left|\mathbf{F}^H\boldsymbol{\Sigma}_T\mathbf{F}\right|}{\left|\mathbf{F}^H\boldsymbol{\Sigma}_C\mathbf{F}\right|} \end{aligned} \tag{2}$$

where dim(•) is the matrix dimension. This can be directly solved using the generalized eigenvalue decomposition (GEVD) method:

$$\boldsymbol{\Sigma}_T f_k = \lambda_k \boldsymbol{\Sigma}_C f_k \tag{3}$$

where λ_k is the *k*-th largest eigenvalue of the GEVD with the corresponding eigenvector f_k and f_k constitutes the k-th column vector of the matrix $\mathbf{F}$. Because $\boldsymbol{\Sigma}_C$ is an invertible matrix according to the definition of the polarimetric covariance matrix, Eq. (3) can be rewritten as

$$\boldsymbol{\Sigma}_C^{-1}\boldsymbol{\Sigma}_T f_k = \lambda_k f_k \tag{4}$$

Thus, the EVD method can be used to obtain a suboptimal solution to the ratio trace problem. Both GEVD and EVD are approximate solutions after converting the trace ratio problem into a ratio trace problem. In Section III.B we listed some the traditional and novel methods of numerical solution for the TR problems are listed.

B. Strict Subspace of PDOF

The objective of PDOF is to enlarge the TCR when reducing clutter fluctuation because both factors affect the detection performance [6]. The standard deviation of clutter fluctuation s/m should be minimized for speckle reduction [10, 19]:

$$\mathrm{s/m} = \frac{\sqrt{\operatorname{tr}(\mathbf{P}\boldsymbol{\Sigma}_C)^2}}{\operatorname{tr}(\mathbf{P}\boldsymbol{\Sigma}_C)} \tag{5}$$

Therefore, in PDOF, the variable M^2 should be maximized to improve the detection performance.

$$M^2 = \left[\frac{TCR}{(\mathrm{s/m})}\right]^2 = \frac{\operatorname{tr}^2(\mathbf{P}\boldsymbol{\Sigma}_T)}{\operatorname{tr}(\mathbf{P}\boldsymbol{\Sigma}_C)^2} \tag{6}$$

With the Hermitian property of $\boldsymbol{\Sigma}_T$ and $\boldsymbol{\Sigma}_C$, there exists $\mathbf{A}^H = \mathbf{A} = \boldsymbol{\Sigma}_T^{\frac{1}{2}}$, $\mathbf{B}^H = \mathbf{B} = \boldsymbol{\Sigma}_C^{\frac{1}{2}}$:

$$\begin{aligned} M^2 &= \frac{\operatorname{tr}^2(\mathbf{P}\boldsymbol{\Sigma}_T)}{\operatorname{tr}(\mathbf{P}\boldsymbol{\Sigma}_C)^2} = \frac{\operatorname{tr}^2(\mathbf{F}\mathbf{F}^H\mathbf{A}\mathbf{A}^H)}{\operatorname{tr}(\mathbf{F}\mathbf{F}^H\mathbf{B}\mathbf{B}^H\mathbf{F}\mathbf{F}^H\mathbf{B}\mathbf{B}^H)} \\ &= \frac{\operatorname{tr}^2(\mathbf{B}^H\mathbf{F}(\mathbf{B}^H\mathbf{F})^H\mathbf{B}^{-1}\mathbf{A}(\mathbf{B}^{-1}\mathbf{A})^H)}{\operatorname{tr}(\mathbf{B}^H\mathbf{F}(\mathbf{B}^H\mathbf{F})^H)^2} \end{aligned} \tag{7}$$

The diagonalization can be performed as follows:

$$\mathbf{B}^H\mathbf{F}(\mathbf{B}^H\mathbf{F})^H = \boldsymbol{\Sigma}_C^{\frac{1}{2}}\mathbf{P}\boldsymbol{\Sigma}_C^{\frac{1}{2}} = \mathbf{U}\boldsymbol{\Lambda}_{PC}\mathbf{U}^H \tag{8.a}$$

$$\mathbf{B}^{-1}\mathbf{A}(\mathbf{B}^{-1}\mathbf{A})^H = \boldsymbol{\Sigma}_C^{-\frac{1}{2}}\boldsymbol{\Sigma}_T\boldsymbol{\Sigma}_C^{-\frac{1}{2}} = \mathbf{V}\boldsymbol{\Lambda}_{TC}\mathbf{V}^H \tag{8.b}$$

where $\mathbf{U}\mathbf{U}^H = \mathbf{V}\mathbf{V}^H = \mathbf{I}_{n\times n}$. $\mathbf{I}_{n\times n}$ is an identity matrix of order n. $\boldsymbol{\Lambda}_{PC} = diag(c_1, c_2, \ldots, c_n)$ $\boldsymbol{\Lambda}_{TC} = diag(b_1, b_2, \ldots, b_n)$. For convenience, $b_1 \ge b_2 \ge \cdots \ge b_n \ge 0$, $c_1 \ge c_2 \ge \cdots \ge c_n \ge 0$.

Eq. (7) becomes

$$M^2 = \frac{\operatorname{tr}^2(\mathbf{V}^H\mathbf{U}\boldsymbol{\Lambda}_{PC}\mathbf{U}^H\mathbf{V}\boldsymbol{\Lambda}_{TC})}{\operatorname{tr}(\boldsymbol{\Lambda}_{PC})^2} \tag{9}$$

The numerator $\operatorname{tr}^2(\mathbf{V}^H\mathbf{U}\boldsymbol{\Lambda}_{PC}\mathbf{U}^H\mathbf{V}\boldsymbol{\Lambda}_{TC})$ reaches a maximum when $\mathbf{U} = \mathbf{V}$ [25]. On this condition:

$$M^2(m) = \frac{\operatorname{tr}^2(\boldsymbol{\Lambda}_{PC}\boldsymbol{\Lambda}_{TC})}{\operatorname{tr}(\boldsymbol{\Lambda}_{PC})^2} = \frac{\left(\sum_{i=1}^{m} b_i c_i\right)^2}{\sum_{i=1}^{m} c_i^2} \le \sum_{i=1}^{m} b_i^2 \tag{10}$$

where b_i is the $i-th$ largest eigenvalue of $\boldsymbol{\Lambda}_{TC}$, and (10) holds and only holds if

$$\frac{b_1}{c_1} = \frac{b_2}{c_2} = \ldots = \frac{b_m}{c_m} \tag{11}$$

Therefore, the projection matrix $\mathbf{P}$ can be derived using Eq. (8.a) and (8.b):

$$\mathbf{P}(m) = \boldsymbol{\Sigma}_C^{-\frac{1}{2}}\mathbf{U}\boldsymbol{\Lambda}_{TC}\mathbf{U}^H\boldsymbol{\Sigma}_C^{-\frac{1}{2}} \tag{12}$$

where the subscript m denotes the dimension of the subspace.

A special case is when $m = n$,

$$\mathbf{P}(n) = \boldsymbol{\Sigma}_C^{-1}\boldsymbol{\Sigma}_T\boldsymbol{\Sigma}_C^{-1} \tag{13}$$

Equation (13) is the representation of PDOF, which means that the SPDOF is a generalization of the PDOF when a subspace is used instead of the full space. In addition, the APDOF in [6] is only an approximation and not a generalized version of the PDOF. When the prior information of $\boldsymbol{\Sigma}_T$ is unknown, we can replace $\boldsymbol{\Sigma}_T$ by $\mathbf{C}$ as the maximum likelihood (ML) estimation, where $\mathbf{C}$ is the polarimetric covariance matrix of the current area. If $m = n$, it becomes a weakened PDOF [6].

C. Statistics of the Subspace Dimension Detectors

The polarimetric detectors based on MCSR and PDOF both have the same mathematical form as follows [6]:

$$z_L = \frac{1}{L}\sum_{i=1}^{L}\mathbf{s}_i^H\mathbf{P}\mathbf{s}_i = \operatorname{tr}(\mathbf{PC}) \tag{14}$$

where $\mathbf{s}_i$ is the scattering vector with dimension d for the $i-th$ pixel, L is the number of looks, and z_L is denoted by a quadratic form. $\mathbf{C}$ is the polarimetric covariance matrix. The difference between the MCSR and PDOF detectors is only the transformation matrix for each detector.

In homogeneous sea state, the polarimetric covariance matrix $\mathbf{C}$ is assumed to be Wishart distributed

$$f_C(\mathbf{C}) = \frac{L^{Ld}\left|\mathbf{C}\right|^{L-d}\exp\left\{-L\,\mathrm{Tr}\left(\mathbf{\Sigma}^{-1}\mathbf{C}\right)\right\}}{\Gamma_d(L)\left|\mathbf{\Sigma}\right|^{L}} \tag{15}$$

where $\Gamma(\bullet)$ denotes gamma function and $\Gamma_d(L)$ is:

$$\Gamma_d(L) = \pi^{\frac{1}{2}d(d-1)}\Gamma(L)\cdots\Gamma(L-d+1) \tag{16}$$

$\mathbf{\Sigma} = \mathrm{E}\left\{\mathbf{C}\right\}$ is the mathematical expectation of the polarimetric covariance matrix, and $\mathrm{E}(\bullet)$ is the expectation operator.

The quadratic form z_L can always be expressed as [26]:

$$z_L \sim \gamma\left(Lb, \frac{a}{L}\right) \tag{17}$$

Here, $\gamma\left(\alpha, \beta\right)$ is the gamma distribution, which can be expressed as follows

$$\gamma(\alpha,\beta) = \frac{1}{\Gamma(\alpha)}\frac{1}{\beta}\left(\frac{x}{\beta}\right)^{\alpha-1}e^{-\frac{x}{\beta}} \tag{18}$$

where α is the shape parameter and β is the scale parameter.

If the detection threshold is assumed to be T, the probability of false alarm (PFA) or probability of detection (PD) can be determined using Eq. (19) [6]:

$$P_{fa/d} = \int_T^{\infty}\gamma(Lb,\frac{a}{L})dz = 1\text{-}\Gamma[Lb,\frac{LT}{a}] \tag{19}$$

where

$$\Gamma(a) = \int_0^{\infty}e^{-t}t^{a-1}dt,\ \Gamma(a,x) = \frac{1}{\Gamma(a)}\int_0^{x}e^{-t}t^{a-1}dt \tag{20}$$

P_{fa} and P_d are the PFA and PD, respectively. When P_{fa} is calculated, $\mathbf{\Sigma} = \mathbf{\Sigma}_C$; when P_d is calculated, $\mathbf{\Sigma} = \mathbf{\Sigma}_T$. When the PFA is fixed, the threshold T can be derived as

$$T = \Gamma^{-1}[Lb, 1\text{-}P_{fa}]a/L \tag{21}$$

where $\Gamma^{-1}[\cdot]$ is the inverse incomplete gamma function [26]. The terms λ_1, λ_2, …, λ_d are the nonzero eigenvalues of $\mathbf{P\Sigma}$. $a = \sum_{i=1}^{d}\lambda_i^2/\sum_{i=1}^{d}\lambda_i$, and $b = \left(\sum_{i=1}^{d}\lambda_i\right)^2/\sum_{i=1}^{d}\lambda_i^2$. In addition, the models can be extended to a generalized gamma distribution (GΓD), which improves the robustness of the statistical model. The results can help to derive the optimal dimension of the subspace detector for trace based detectors. The proposed algorithm is built in Section III.C.

D. Modified Linear Discriminant Analysis

Different subspace detectors extract the different nonlinear characteristics of the ship detectors. If they can be fused together, the detection performance can be improved. Therefore, we propose a modified linear discriminant analysis (MLDA) method based on LDA and improved GOPCE [21] to combine the subspaces of MCSR and PDOF detectors. We define the objective function as

$$\underset{\|\mathbf{x}\|=1}{\mathrm{argmax}}\,J(\mathbf{x}) = \frac{\mathrm{E}(\mathbf{x}^T\mathbf{z}_T)^2 - \mathrm{E}(\mathbf{x}^T\mathbf{z}_C)^2}{\mathrm{Var}(\mathbf{x}^T\mathbf{z}_C)+\mathrm{Var}(\mathbf{x}^T\mathbf{z}_T)} \tag{22}$$

The $\mathbf{z}$ = (z_{SPDOF} , z_{APDOF} , z_{ITR} , z_{EVD}) composes the Fisher vector, $\mathbf{z}_T$ is for targets, $\mathbf{z}_C$ is for clutter, and $\mathbf{x}$ denotes the weight coefficient. In traditional LDA, the between-class distance is $\left(\mathrm{E}(\mathbf{x}^T\mathbf{z}_T) - \mathrm{E}(\mathbf{x}^T\mathbf{z}_C)\right)^2$, and it is simplified to a new form as $\mathrm{E}(\mathbf{x}^T\mathbf{z}_T)^2 - \mathrm{E}(\mathbf{x}^T\mathbf{z}_C)^2$ in Eq. (22), which is validated to perform better [21]. $\mathrm{Var}\left(\bullet\right)$ is the variance operator and $\left\|\bullet\right\|$ is the norm operator. It can be simplified as

$$\underset{\|\mathbf{x}\|=1}{\mathrm{argmax}}\,J(\mathbf{x}) = \frac{\mathbf{x}^T(\mathbf{R}_T - \mathbf{R}_C)\mathbf{x}}{\mathbf{x}^T(\mathbf{R}_C - \boldsymbol{\mu}_C\boldsymbol{\mu}_C^T)\mathbf{x} + \mathbf{x}^T(\mathbf{R}_T - \boldsymbol{\mu}_T\boldsymbol{\mu}_T^T)\mathbf{x}} \tag{23}$$

where $\mathbf{R}_T$ and $\mathbf{R}_C$ are the feature covariance matrices, and $\boldsymbol{\mu}_C$ and $\boldsymbol{\mu}_T$ are the mean feature vectors, respectively. We extend it to multidimensional subspaces as follows:

$$\underset{\mathbf{Q}^H\mathbf{Q}=\mathbf{I}}{\mathrm{argmax}}\,J(\mathbf{G}) = \frac{\mathrm{tr}(\mathbf{GR}_T) - \mathrm{tr}(\mathbf{GR}_C)}{\mathrm{tr}(\mathbf{G}(\mathbf{R}_C - \boldsymbol{\mu}_C\boldsymbol{\mu}_C^T))+\mathrm{tr}(\mathbf{G}(\mathbf{R}_T - \boldsymbol{\mu}_T\boldsymbol{\mu}_T^T))} \tag{24}$$

where $\mathbf{G}=\mathbf{QQ}^H$, and $\mathbf{Q}^H\mathbf{Q}=\mathbf{I}$. This is similar to the projection matrix $\mathbf{P}$, which may not be a square matrix.

To balance the clutter variance and target variance, the parameter β is added to the objective function as follows:

$$\underset{\mathbf{Q}^H\mathbf{Q}=\mathbf{I}}{\mathrm{argmax}}\,J(\mathbf{G}) = \frac{\mathrm{tr}(\mathbf{GR}_T) - \mathrm{tr}(\mathbf{GR}_C)}{\mathrm{tr}(\mathbf{GR}_{SC})+\beta\mathrm{tr}(\mathbf{GR}_{TC})} \tag{25}$$

where $\mathbf{R}_{SC}=\mathbf{R}_C - \boldsymbol{\mu}_C\boldsymbol{\mu}_C^T$, $\mathbf{R}_{TC}=\mathbf{R}_T - \boldsymbol{\mu}_T\boldsymbol{\mu}_T^T$ and β is the balance factor between the sample numbers of the clutter and targets. To adapt to the complex clutter background, $l_{2,p}$ norm regularization can be used to capture general features [27]. The coefficient $\mathrm{tr}(\mathbf{GR}_C)$ can be used to adjust the whitening contribution. Therefore, the objective function becomes:

$$\underset{\mathbf{Q}^H\mathbf{Q}=\mathbf{I}}{\mathrm{argmax}}\,J(\mathbf{G}) = \frac{\mathrm{tr}(\mathbf{GR}_T) + \lambda\mathrm{tr}(\mathbf{GR}_C)}{\mathrm{tr}(\mathbf{GR}_{SC})+\beta\mathrm{tr}(\mathbf{GR}_{ST}) + \gamma\left\|\mathbf{G}\right\|_{2,p}} \tag{26}$$

where, λ, β, and γ are all balance parameters, p is a regularization parameter. It is called the modified linear discriminant analysis (MLDA), which unified both Novak's principle and the LDA algorithm. The MLDA also becomes a trace ratio problem, whose calculation can be found in [27]. The joint subspace detector can be expressed as $\mathrm{tr}(\mathbf{GR})$. $\mathbf{R}$ is the observed covariance matrix of features.

E. Diagonal Loading Method in PDOF

Many polarimetric detectors exist. The SPDOF and APDOF have similar forms among the four polarimetric detectors presented here. The only difference is the choice of the diagonal elements of a matrix. As shown in Section III, the combination of SPDOF and PDOF by the MLDA method always yields the best performance among all the detector combinations. This phenomenon motivated us to propose a novel detector by combining SPDOF and APDOF directly.

The APDOF form is [6]

$$\mathbf{P} = \mathbf{\Sigma}_C^{-1/2}\mathbf{U}\mathbf{\Lambda}_{GC}\mathbf{U}^H\mathbf{\Sigma}_C^{-1/2} \tag{27}$$

and the SPDOF is

$$\mathbf{P} = \mathbf{\Sigma}_C^{-\frac{1}{2}} \mathbf{U} \mathbf{\Lambda}_{TC} \mathbf{U}^H \mathbf{\Sigma}_C^{-\frac{1}{2}} \tag{28}$$

where $\mathbf{\Lambda}_{GC} = \begin{bmatrix} \mathbf{I}_{m\times m} & \mathbf{0} \\ \mathbf{0} & \mathbf{0} \end{bmatrix}_{n\times n}$ if the subspace dimension is m.

From Eq. (27-28), it can be found that the unique difference between them is the choice of the diagonal matrix. Therefore, we can build a novel detector by combining the SPDOF and APDOF as follows:

$$\mathbf{P} = \mathbf{\Sigma}_C^{-1/2} \mathbf{U} \left(\mathbf{\Lambda}_{TC} + \eta \mathbf{\Lambda}_{GC} \right) \mathbf{U}^H \mathbf{\Sigma}_C^{-1/2} \tag{29}$$

where η is the loading factor. Because the diagonal matrix is formed by an eigenvalue matrix $\mathbf{\Lambda}_{TC}$ plus an identity matrix $\mathbf{\Lambda}_{GC}$, we call the novel detector the diagonal loading detector (DLD). The balance parameter η is very important for improving detection performance. To search for an accurate value efficiently, the initial value can be derived from the MLDA method, which combines SPDOF and APDOF together.

In addition, the GEVD method can be considered as the other form of APDOF. Equation (3) can be transformed as

$$\mathbf{\Sigma}_C^{-\frac{1}{2}} \mathbf{\Sigma}_T \mathbf{\Sigma}_C^{-\frac{1}{2}} \left(\mathbf{\Sigma}_C^{\frac{1}{2}} f_k \right) = \lambda_k \left(\mathbf{\Sigma}_C^{\frac{1}{2}} f_k \right) \tag{30}$$

where $\mathbf{U} = \mathbf{\Sigma}_C^{\frac{1}{2}} \mathbf{F}$, $\mathbf{F} = \left[f_1, \ldots f_m \right]$. As a result, we get

$$\mathbf{P} = \mathbf{F}\mathbf{F}^H = \mathbf{\Sigma}_C^{-\frac{1}{2}} \mathbf{U} \mathbf{U}^H \mathbf{\Sigma}_C^{-1/2} \tag{31}$$

Therefore, the GEVD is the same as the APDOF, which provides a new explanation. It should also be noted that the EVD can only provide an approximate solution to the ratio trace problem. In the following experiments, the GEVD detector was replaced by the APDOF detector.

In addition, if the APDOF is full dimension, the APDOF becomes a PWF. Then, the DLD of the full dimension becomes a linear combination of the PDOF and PWF.

III. EXPERIMENTS VIA SIMULATION

A. Simulated Data Generation

A high-dimensional vector was established for ship detection based on the neighborhood polarimetric covariance matrix (NPCM), derived from the cross product of high-dimensional vectors conforming to a complex Gaussian distribution [28]. Therefore, NPCM can be used to validate the proposed method. The NPCM was established in seven different neighborhood forms [28]. Here, the horizontal-vertical neighborhood form (Fig. 2(a)) is used to establish a 15-dimensional covariance matrix. The simulated data were generated using the Monte Carlo method with underlying statistics obtained from a real dataset [6]. It should be noted that the NPCM is not necessary. It can also be made by the coefficients of different polarimetric decompositions [14], or the 3-dimensional polarimetric covariance matrix, as shown in the measured dataset. We can also find that the high dimension may improve the detection performance.

The data generation method is the same as in [6]. In the simulation, $N = 100{,}000$ samples were generated by a Monte Carlo method. Three common statistical models of clutter, including Wishart, $\mathcal{K}$ distribution, and $\mathcal{G}_0$ distribution, are used with the true polarimetric covariance matrix $\mathbf{\Sigma}_C$ [29]. Targets obey a $\mathcal{G}_0$-distribution with the expectation of a polarimetric covariance matrix $\mathbf{\Sigma}_T$ [29]. Both $\mathbf{\Sigma}_C$ and $\mathbf{\Sigma}_T$ were drawn from RadarSat-2 data [6]. The multi-look number L was set to 4. The shape parameters of the $\mathcal{K}$-distribution and $\mathcal{G}_0$-distribution are 10 for the clutter. For ship targets, the shape parameter of the $\mathcal{G}_0$-distribution was 2. The TCR is defined as

$$\text{TCR} = \text{tr}(\mathbf{\Sigma}_T) / \text{tr}(\mathbf{\Sigma}_C) \tag{32}$$

where $\text{tr}(\mathbf{\Sigma}_T)$ denotes the power of the targets, $\text{tr}(\mathbf{\Sigma}_C)$ denotes the clutter power, and $\mathbf{\Sigma}_T = \mathbf{\Sigma}_C + \mathbf{\Sigma}_t$. Here the TCR is 1.5 and the Pauli RGB images are presented in Fig. 2(b-f).

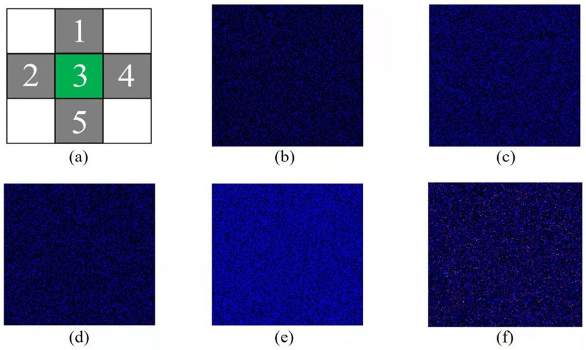

Fig. 2. NPCM and Pauli images of the simulated dataset: (a) NPCM (b) clutter pixels of Wishart (c) clutter pixels of K-Wishart (d) clutter pixels of G0-Wishart (e) ship pixels of Wishart (f) ship pixels of G0-Wishart

B. Efficiency of the TR problem Solution

For the trace ratio itself, we propose an effective solver based on score evaluation using an iterative method. In a previous study [23], an iterative algorithm called ITR was proposed to solve (1), while a more efficient method was proposed in [24] and named the ITR-score algorithm. In a separate study [22], the suboptimal EVD solution was set as the initial value, improving the algorithm efficiency. Here, the ITR-score algorithm is used to efficiently find the eigenvector. The combined algorithm can be called an improved ITR-score (IITR-score) algorithm. The basic steps of the IITR-score algorithm are listed in Table I.

TABLE I
AN IMPROVED ITR-SCORE ALGORITHM FOR THE TR PROBLEM

```
(1) Calculate the suboptimal solution of MCSR problem, obtain the matrix $\mathbf{F}_0$,
    and calculate the initial value $\tau_1 = \text{tr}(\mathbf{F}_0^H \mathbf{\Sigma}_T \mathbf{F}_0) / \text{tr}(\mathbf{F}_0^H \mathbf{\Sigma}_C \mathbf{F}_0)$.
(2) Computer the eigen-decomposition of $\mathbf{\Sigma}_T - \tau_t \mathbf{\Sigma}_C$ : $(\mathbf{\Sigma}_T - \tau_t \mathbf{\Sigma}_C) f_i = \lambda_i f_i$,
    where $u_i (i = 1, 2, \cdots, n)$ is the eigenvector of $\mathbf{\Sigma}_T - \tau_t \mathbf{\Sigma}_C$.
(3) Compute the score $s_i = f_i^H \mathbf{\Sigma}_T f_i / f_i^H \mathbf{\Sigma}_C f_i$ for each eigenvector $f_i$
(4) Choose the top $m$ eigenvectors $f_i$ having the $m$ largest eigenvalues $f_i$
    to form $\mathbf{F}_t$.
(5) Update $\tau_{t+1} = \text{tr}(\mathbf{F}_t^H \mathbf{\Sigma}_T \mathbf{F}_t) / \text{tr}(\mathbf{F}_t^H \mathbf{\Sigma}_C \mathbf{F}_t)$.
(6) Iterate the steps (2-5) until $\left| \tau_{t+1} - \tau_t \right| < \varepsilon$, Output $\hat{\mathbf{F}} = \mathbf{F}_{t+1}$.
```

Here, five methods to solve the trace ratio problem are compared using the Monte Carlo method: MCSR-Y [14], IITR [22], ITR-score [24], and IITR-score. The absolute bias ε and computation time (s) are listed in Table II. The ε in Table I is set as 1e-6, and the repetition times are 1e4. The dimension of the feature vector is 15, and the subspace dimension is 5. It can be seen that the IITR gives the best performance, and we also find that the number of recycle times of the IITR-score is the lowest in the simulation. It also shows that a suitable initial value significantly affects the calculation efficiency.

TABLE II
THE COMPARISON OF SOLUTIONS FOR TRACE RATIO PROBLEM

	MCSR-Y	IITR-score	ITR-score	IITR
Bias	5e-6	1e-6	1e-6	1e-6
time cost (s)	0.0012	0.0033	0.0054	0.0009
recycles	8	4	7	4

C. *The Optimal Subspace of Different Detectors*

Defining the optimal subspace dimension is an interesting problem for ship detection. In this work, we solve this problem using a statistical model and AUC. The AUC allows the assessment of the performance of different dimensional subspaces to determine the optimal dimension of the polarimetric detection subspace. We used the analytical expressions of P_{fa} and P_d derived for a Wishart distribution to calculate the AUC. The algorithm is presented in Table III.

TABLE III
ALGORITHM TO DERIVE THE OPTIMAL DIMENSION

(1) Solve the subspace projection matrix $\mathbf{P}$ for one subspace.
(2) Calculate the a_C , b_C , a_T , b_T for clutter and targets, respectively, in Eq. (19).
(3) Set P_{fa} =[1e-8,1]. Calculate the threshold range $\mathscr{H}$ in Eq. (21).
(4) Calculate P_d in Eq. (19) with the range $\mathscr{H}$.
(5) Calculate the AUC for each subspace of the different dimension m .
(6) Repeat (1-5) until all the subspaces are covered.
(7) Choose the optimal dimension by the largest AUC among all the subspace projection matrices.

1) *The Optimal Subspace of the MCSR*

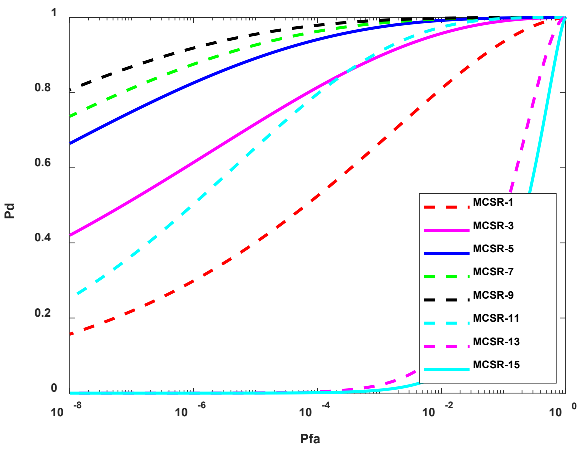

Fig. 3. ROC curves by numerical calculation when TCR = 1. 2.

We used receiver of characteristics (ROC) curves to plot quantitative results about the performance of detectors using the analytical expressions derived previously (Fig. 3). "Pd" is the probability of detection (PD), "Pfa" is the probability of false alarm (PFA). "MCSR-*m*" denotes the *m*-dimensional MCSR (TR) subspace. The 9-dimensional subspace provides the best detection performance, regardless of whether the target clutter ratio (TCR) is small or large.

Fig. 4 shows the results obtained using the Monte Carlo simulations. In Fig. 3(a), both the clutter and targets are Wishart-distributed (CWTW). These results are consistent with the theoretical results shown in Fig. 3. In Fig 4(b), the clutter is still Wishart-distributed, but the targets are set as $\mathcal{G}_0$ -distributed (CWTG) [6] to study the robustness of the algorithm. In this case, dimension 9 was still the best. In Fig. 4(c), the clutter is $\mathcal{K}$ distributed and targets are $\mathcal{G}_0$ distributed (CKTG); the optimal dimension in this case is 5. When the clutter is $\mathcal{G}_0$ distributed and targets are also $\mathcal{G}_0$ distributed (CGTG), the optimal dimension is 5.

The higher the TCR is, the better the detection performance is. In the simulations, some of the plots have TCR = 1.5, and some TCR = 1.2, because in some cases of 1.5, the curves will be too high. The fitting of the statistical model also affects the detection results. When the actual targets and clutter statistics are Wishart distributed, consistency is evident. When their actual distribution is different from that of Wishart, the algorithm can still perform adequately, but the solution for the optimal subspace dimension is not the best one.

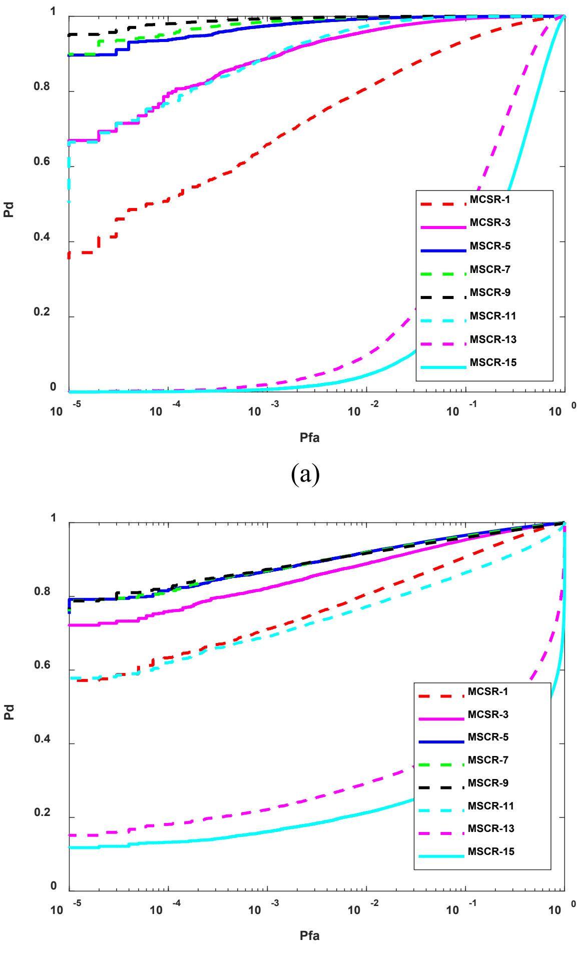

(a)

(b)

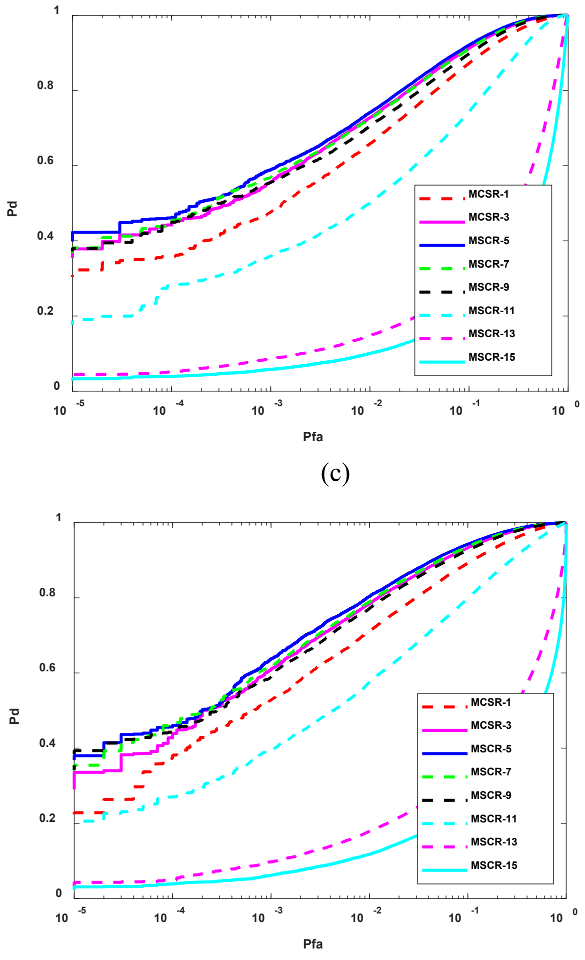

(c)

(d)

Fig. 4. ROC curves by Monte Carlo simulation. (a) CWTW TCR = 1.2 (b) CWTG TCR = 1.5 (c) CKTG TCR = 1.5 (d) CGTG TCR = 1.5.

2) The Optimal Subspace of the PDOF

In the PDOF, the results from the analytical solution are presented in Fig. 5, while the results for the Monte Carlo simulation data are shown in Fig 6. "PDOF-*m*" denotes the *m*-dimensional PDOF subspace.

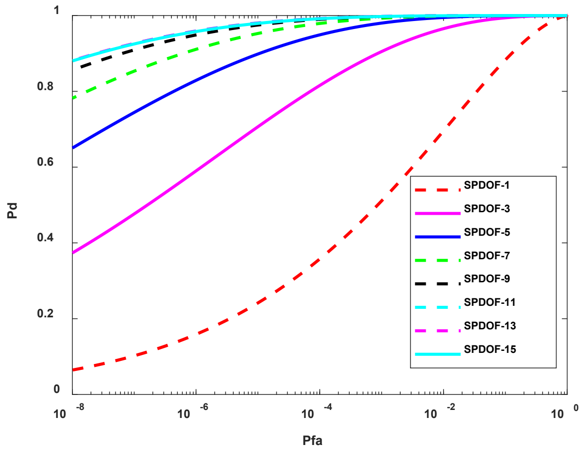

Fig. 5. ROC curves by numerical calculation when TCR = 1.15.

It can be seen that PDOF-9–PDOF-15 achieves the best performance and PDOF-1 achieves the worst performance when the clutter is Wishart, as shown in Fig. 6 (a) and (b).

These results are consistent with this theory. When sea clutter becomes more heterogeneous, the optimal dimension of the PDOF is 5, regardless of whether the clutter statistics is $\mathcal{K}$ or $\mathcal{G}_0$.

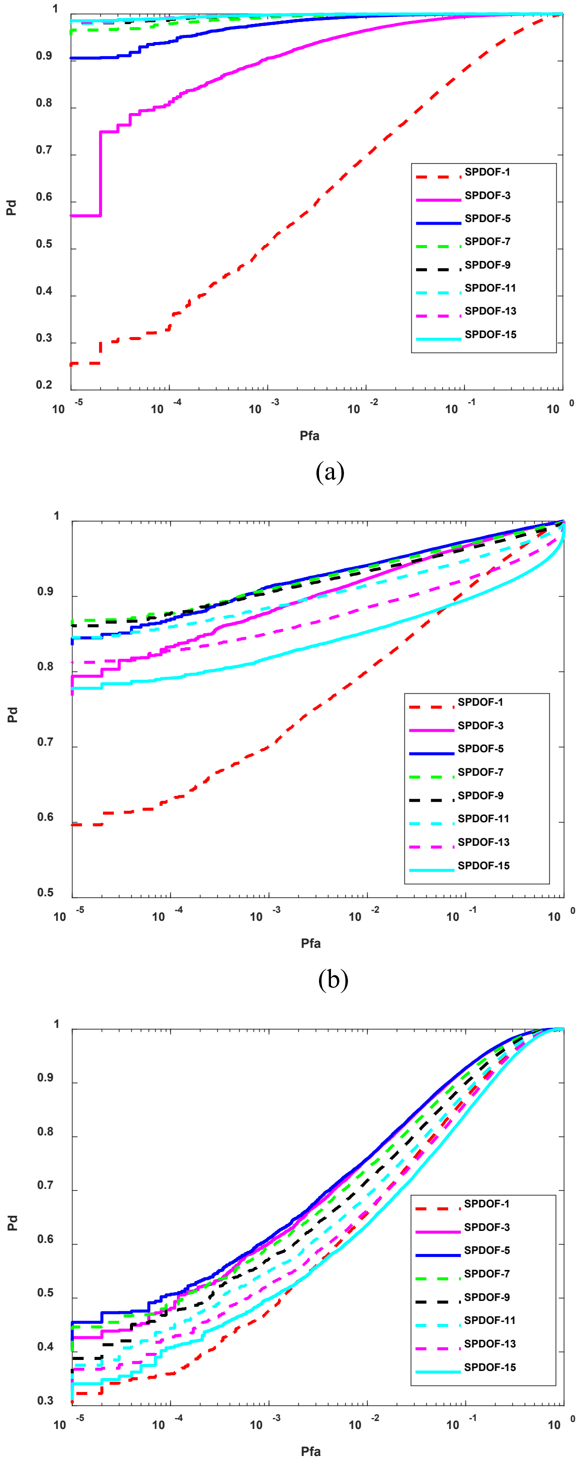

(a)

(b)

(c)

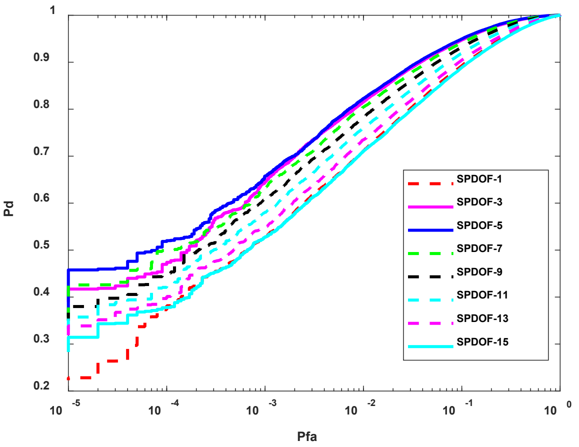

(d)

Fig. 6. ROC curves by Monte Carlo simulation. (a) CWTW TCR = 1.15 (b) CWTG TCR = 1.5 (c) CKTG TCR = 1.5 (d) CGTG TCR = 1.5.

D. *Performance Analysis of Joint Subspaces Detector*

Here, the detection performance of the joint subspace detector is presented. The combination includes four subspaces: SPDOF, APDOF, MCSR, and EVD. Because the optimal dimension for each subspace is similar in our simulations, we chose this dimension for the MCSR to be 9 in a homogeneous background and 5 in a heterogeneous background. The balance parameters are initially defined as $\lambda=0$, $\beta=0$, $\gamma=0$, $p=2$, and $d=15$. In the following figures, “Detector-*m*” denotes the subspace detection with the dimension *m* and “Joint-*m*” denotes the joint subspace detector with dimension *m*. The area under curves (AUCs) are presented in the following Tables. In these tables, the results with different parameters are provided using the same background. $\lambda=-1$ indicates that the initial $\lambda=0$ change is -1. $\beta=1$ indicates that the initial $\beta=0$ change is 1. $\gamma=1$ means changing the initial $\gamma=0$ value to 1. $p=1$ means changing the initial $p=2$ value to 1 and $\gamma=1$ to 1. $d=9$ means changing the subspace dimension $d=15$ to 9. When one parameter is changed, the others remain the same as before.

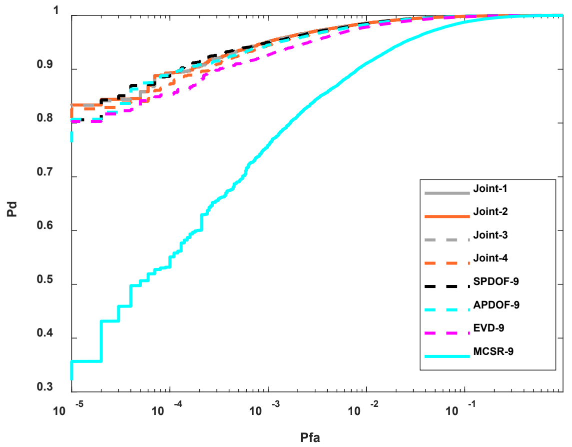

Fig. 7. Comparisons of joint subspaces detectors: ROCs of different polarimetric subspace detectors (CWTW TCR = 1.1).

TABLE IV
AUCS OF DIFFERENT POLARIMETRIC SUBSPACE DETECTORS

	Normal	$\lambda=-1$	$\beta=1$	$\gamma=1$	$p=1$	$d=9$
Joint-1	0.9992	0.9993	0.9962	0.9991	0.9991	0.9992
Joint-2	0.9992	0.9993	0.9962	0.9991	0.9990	0.9992
Joint-3	0.9992	0.9993	0.9965	0.9991	0.9990	0.9991
Joint-4	0.9990	0.9990	0.9990	0.9990	0.9990	0.9992
SPDOF-9			0.9992			
APDOF-9			0.9991			
EVD-9			0.9987			
MCSR-9			0.9943			

In Fig. 7 and 8, the detection ROCs with initial parameters are presented in the CWTW and CWTG cases, respectively, where the TCR is 1.1 and 1.5. It can be seen that SPDOF-9 provides the best performance, and the MCSR gives the worst performance. The remaining detectors provided approximately the same performance. In Tables IV and V, “Joint-4” is the most stable detector with respect to the changing parameters. It can also be seen that the normal parameters give the best performance when we vary only one and leave the other the same from all these tables.

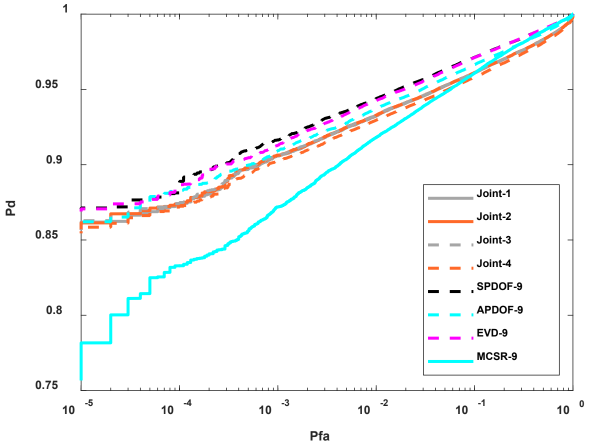

Fig. 8. Comparisons of joint subspaces detectors: ROCs of different polarimetric subspace detectors (CWTG TCR = 1.5).

TABLE V
AUCS OF DIFFERENT POLARIMETRIC SUBSPACE DETECTORS

	Normal	$\lambda=-1$	$\beta=1$	$\gamma=1$	$p=1$	$d=9$
Joint-1	0.9798	0.9798	0.9694	0.9790	0.9787	0.9851
Joint-2	0.9799	0.9799	0.9623	0.9787	0.9778	0.9852
Joint-3	0.9799	0.9799	0.5411	0.9785	0.9778	0.9852
Joint-4	0.9778	0.9778	0.9778	0.9778	0.9778	0.9840
SPDOF-9			0.9866			
APDOF-9			0.9839			
EVD-9			0.9866			
MCSR-9			0.9831			

Fig. 9 and 10 present the detection results with initial parameters and TCR = 1.5. The background is CKTG and CGTG respectively. From these figures it can be seen in the heterogeneous background the Joint-1, Joint-2 and Joint-3 give the best performances, while Joint-4 gives a worse performance, which is comparable to the single subspace detector. The SPDOF performs best among the single detectors.

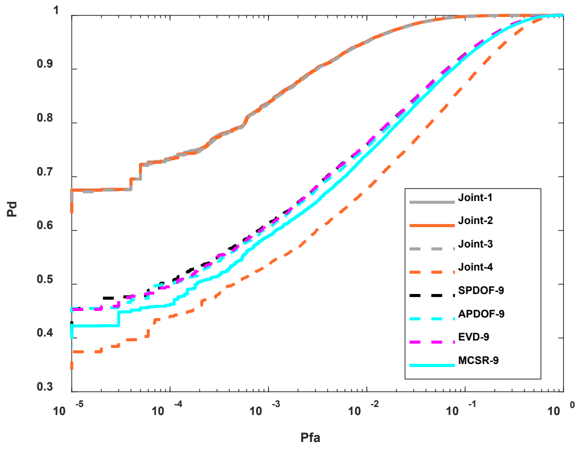

Fig. 9. ROCs of different subspace (CKTG TCR = 1.5).

TABLE VI
AUCS OF DIFFERENT POLARIMETRIC SUBSPACE DETECTORS

	Normal	$\lambda=-1$	$\beta=1$	$\gamma=1$	$p=1$	$d=5$
Joint-1	0.9980	0.9980	0.8900	0.9966	0.9972	0.9768
Joint-2	0.9980	0.9980	0.9735	0.9950	0.9964	0.9770
Joint-3	0.9979	0.9979	0.9951	0.9931	0.9956	0.9770
Joint-4	0.9580	0.9580	0.9580	0.9580	0.9580	0.9761
SPDOF-5	0.9761					
APDOF-5	0.9752					
EVD-5	0.9761					
MCSR-5	0.9735					

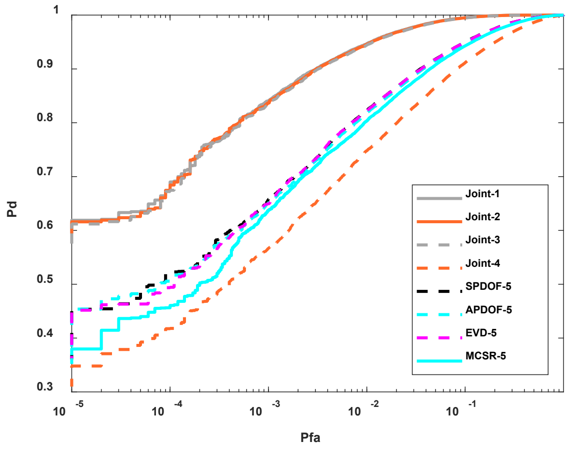

Fig. 10. ROCs of different subspace (CGTG TCR = 1.5).

TABLE VII
AUCS OF DIFFERENT POLARIMETRIC SUBSPACE DETECTORS

	Normal	$\lambda=-1$	$\beta=1$	$\gamma=1$	$p=1$	$d=5$
Joint-1	0.9973	0.9973	0.6933	0.9945	0.9956	0.9764
Joint-2	0.9972	0.9972	0.5835	0.9917	0.9941	0.9794
Joint-3	0.9971	0.9971	0.6051	0.9891	0.9927	0.9794
Joint-4	0.9668	0.9668	0.9668	0.9668	0.9668	0.9819
SPDOF-5	0.9819					
APDOF-5	0.9811					
EVD-5	0.9818					
MCSR-5	0.9790					

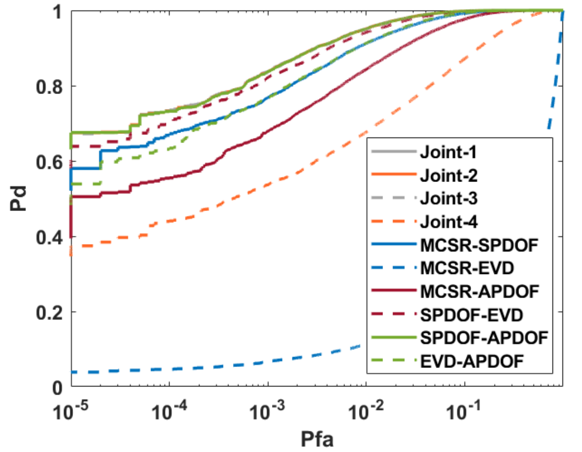

Fig. 11. ROCs of two subspace combination (CKTG).

The joint detectors applied four transform matrices. The two matrices are accurate, and the other two are approximate. Therefore, we used only two subspace combination detectors to observe the detection results to determine the main contribution matrices. The detection results for the CKTG and CGTG cases are presented in Fig. 11-12 and Table VIII-IX. "Detector-detector" denotes the names of the two combinations. "SPDOF-APDOF" gave the best performance among all the two-subspace combined detectors, followed by the "SPDOF-EVD," while that of "MCSR-EVD" was the worst. "SPDOF-APDOF" performed as good as the best joint detectors. As shown in Table VIII-IX, performance was better when the dimensions of the subspaces were not further reduced.

TABLE VIII
AUCS OF DIFFERENT POLARIMETRIC SUBSPACE DETECTORS
(CKTG)

	Normal	$\lambda=-1$	$\beta=1$	$\gamma=1$	$p=1$	$d=5$
M-S	0.9956	0.9957	0.9740	0.9701	0.9766	0.9763
M-E	0.5339	0.5340	0.5467	0.5219	0.5209	0.9762
M-A	0.9908	0.9908	0.9529	0.9283	0.9399	0.9758
S-E	0.9974	0.9974	0.9052	0.9603	0.9615	0.9760
S-A	0.9979	0.9979	0.9955	0.9965	0.9972	0.9770
E-A	0.9959	0.9959	0.8656	0.9118	0.9127	0.9761

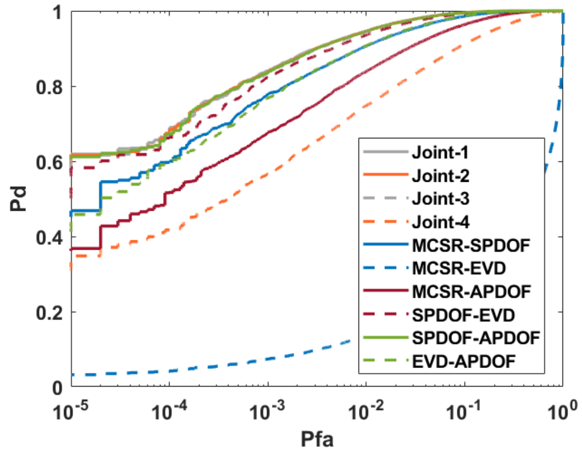

Fig. 12. ROCs of two subspace combination (CGTG).

TABLE IX
AUCS OF DIFFERENT POLARIMETRIC SUBSPACE DETECTORS (CGTG)

	Normal	$\lambda=-1$	$\beta=1$	$\gamma=1$	$p=1$	$d=5$
M-S	0.9941	0.9941	0.6035	0.9729	0.9763	0.9815
M-E	0.5021	0.5020	0.5511	0.4919	0.4910	0.9809
M-A	0.9870	0.9870	0.6640	0.9310	0.9367	0.9808
S-E	0.9965	0.9966	0.6234	0.9684	0.9688	0.9806
S-A	0.9972	0.9972	0.6059	0.9944	0.9956	0.9794
E-A	0.9944	0.9944	0.7205	0.9224	0.9215	0.9818

Here, M, S, E, and A are the abbreviations of MCSR, SPDOF, EVD, and APDOF, respectively. We also note that β will affect the detection performance significantly when the TCR is very large, as can also be seen in the experiments using measured data.

E. Performance Analysis of Diagonal Loading Detector

In our four detectors, SPDOF and APDOF played more important roles because the combination of these two detectors provides the best performance among all the two detector combinations. We extended this result to build a new joint detector by linearly combining SPDOF and APDOF, which was previously named DLD. When the loading factor is negative, we refer to it as a diagonally reducing case.

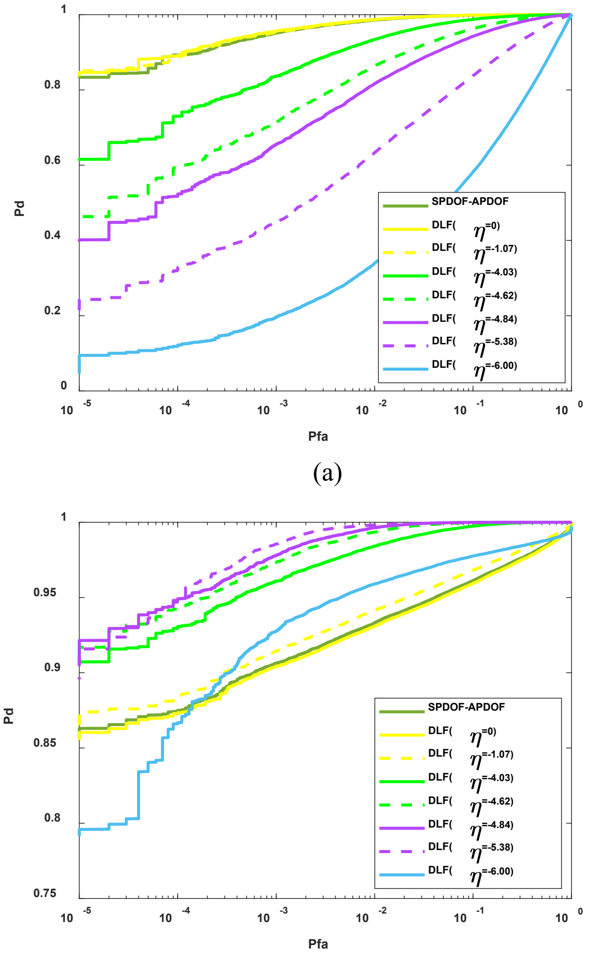

(a)

(b)

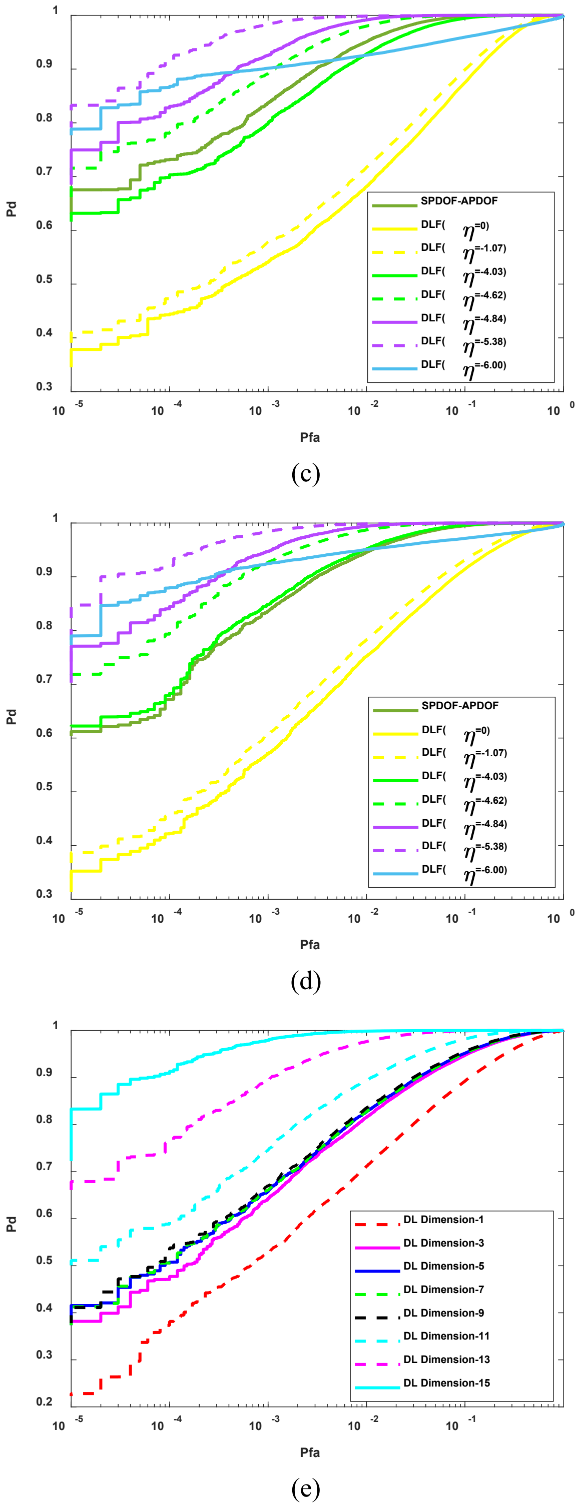

(c)

(d)

(e)

Fig. 13. Comparison of performance among different backgrounds, DL factors, and subspace dimensions: (a) CWTW TCR = 1.1 (b) CWTG TCR = 1.5 (c) CKTG TCR = 1.5 (d) CGTG TCR = 1.5 (e) Results of joint subspace dimension TCR = 1.5.

In the simulation, the statistics of the targets and clutter obey the CWTW, CWTG, CKTG, and CGTG assumptions. The diagonal reducing factors varied from -40 to 0. When the factor is zero, the DLD becomes the SPDOF detector. The AUCs of the ROCs in the different situations are presented in Table IX.

From the figures and tables, it can be seen that if a suitable value for the diagonal loading factor is improved, then the detection performance is improved significantly. DLD manages to almost solve the limitations when the clutter is not Wishart and reaches the performance of the Wishart hypothesis. Here, the diagonal loading factor (DLF) was -5.38. This factor η_{opt} is difficult to determine.

The MLDA solution of the joint SPDOF and APDOF can provide a satisfactory initial value. In Table X, the relations between η_{opt} and the eigenvalues of $\mathbf{\Sigma}_C^{-1}\mathbf{\Sigma}_T$ are presented.

In the simulation, the statistics of the targets and clutter obey the CWTW, CWTG, CKTG, and CGTG assumptions. The diagonal reducing factors varied from -40 to 0. When the factor is zero, the DLD becomes the SPDOF detector. The AUCs of the ROC curves in the different situations are presented in Table X. From the figures and tables, it can be seen that if a suitable value for the diagonal loading factor is improved, then the detection performance is improved significantly. DLD manages to almost solve the limitations when the clutter is not Wishart and reaches the performance of the Wishart hypothesis. Here, the diagonal loading factor (DLF) was -5.38. This factor η_{opt} is difficult to determine. The MLDA solution of the joint SPDOF and APDOF can provide a satisfactory initial value. In Table XI, the relations between η_{opt} and the eigenvalues of $\mathbf{\Sigma}_C^{-1}\mathbf{\Sigma}_T$ are presented.

TABLE X
AUCS OF DIFFERENT POLARIMETRIC SUBSPACE DETECTORS (CGTG)

	η=0	η=-4.03	η=-4.62	η=-5.38
CWTW	0.9993	0.9949	0.9857	0.9362
CWTG	0.9787	0.9990	0.9997	0.9998
CKTG	0.9591	0.9966	0.9992	0.9998
CGTG	0.9679	0.9977	0.9994	0.9998

In Table X, we can see that in our simulation, η_{opt} is in the interval between the mean of the negative eigenvalue $-\overline{b}$ and the mean of the maximum and minimum eigenvalues $-\frac{b_{\max}+b_{\min}}{2}$. $b_{\max}$ and $b_{\min}$ are the maximum and minimum eigenvalues of the matrix, respectively $\mathbf{\Sigma}_C^{-1}\mathbf{\Sigma}_T$. When the TCR is low, the clutter energy is an important factor that affects the detection performance. DL processing has the potential to zero clutter energy. From Eq. (29), we can derive the clutter energy as:

$$\begin{aligned}\operatorname{tr}(\mathbf{P\Sigma}_C) &= \operatorname{tr}(\mathbf{\Sigma}_C{}^{-1/2}\mathbf{U}\left(\mathbf{\Lambda}_{TC}+\eta\mathbf{\Lambda}_{GC}\right)\mathbf{U}^H\mathbf{\Sigma}_C{}^{-1/2}\mathbf{\Sigma}_C) \\ &= \operatorname{tr}\left(\mathbf{\Lambda}_{TC}+\eta\mathbf{\Lambda}_{GC}\right)=\sum_{i=1}^{m}\left(b_i+\eta\right)=\sum_{i=1}^{m}b_i+m\eta=0\end{aligned} \tag{33}$$

That is, $\eta_{\text{opt}}=-\overline{b}$. If TCR is too large, the DLF will be positive, as can be seen in the measured data.

TABLE XI
THE RELATIONS FOR THE OPTIMAL DLF η_{opt} SELECTION (CGTG)

TCR	η_{opt}	$-\frac{b_{\max}+b_{\min}}{2}$	$-\overline{b}$	Ratio(MLDA)
1.1	-1.72	-1.88	-1.72	-1.47
1.2	-2.45	-2.75	-2.45	-2.14
1.3	-3.17	-3.63	-3.17	-2.87
1.4	-4.50	-4.50	-3.89	-3.38
1.5	-5.38	-5.38	-4.62	-4.03
1.6	-6.26	-6.26	-5.35	-4.68
1.7	-6.07	-7.14	-6.07	-5.23
1.8	-6.80	-8.01	-6.80	-5.96
1.9	-8.89	-8.89	-7.52	-6.60
2.0	-9.77	-9.77	-8.24	-7.19

IV. VALIDATION BY MEASURED DATA

A. *Flow chart of experiments*

The flow chart of the joint subspace detector proposed in this study is presented in Fig. 14.

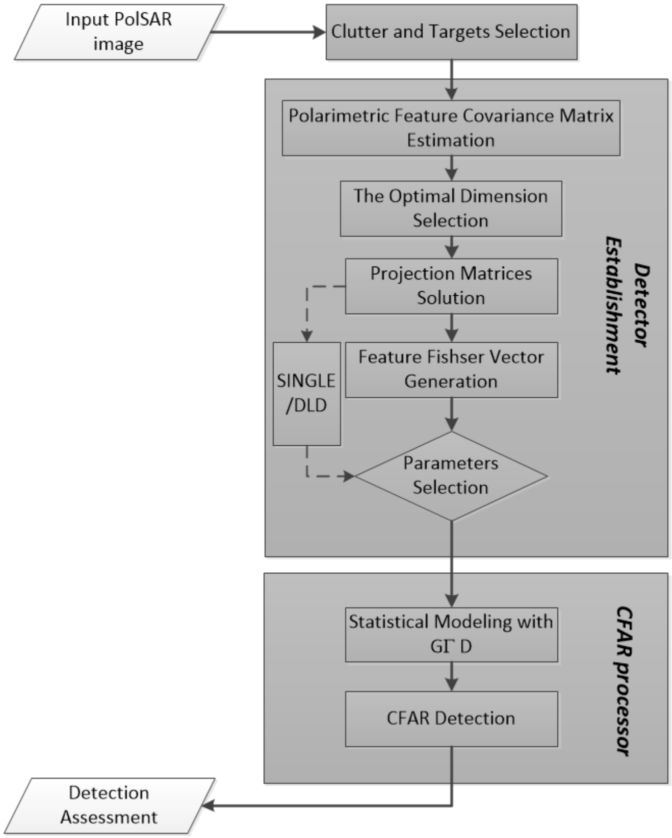

Fig. 14. Workflow of the Joint subspaces detector.

There are four important processes, including initial target selection, detector pre-processing, constant false alarm rate (CFAR) processor, and performance assessment. Detector pre-processing includes estimating the feature covariance matrix, optimal dimension selection, projection matrix solution, feature Fisher vector construction, and parameter selection of the joint detector. The workflow is indicated by the solid arrow lines. Solid parallelograms represent the main inputs and outputs. The rectangular boxes within the gray background regions show the operation and procedure, and diamond is the decision on the balance parameters. The dotted arrow line indicates a parallel process using one type of polarimetric detector, such as SPDOF and DLD. In the MLDA case, β=1e6 is a different ordinary value of *b*, because in the measured dataset, TCR is generally much larger than that we simulated.

B. Measured Data Descriptions

The first scene of real data represents the North Sea area from RADARSAT-2 (RS-2) during November 2013 [6]. Automatic identification system (AIS) positions of the vessels were acquired and used for validation. The scene presents 11 ships, as shown in Fig. 15(a) by PolSAR pro 6.0. "S*n*" denotes the *n*-th ship in the image. A yellow rectangle is used for large ships, and a yellow circle is used for small ships. The wind speed is 32 knots; therefore, the sea state is high [6].

The second and third measured dataset were acquired by NASA/JPL Airborne SAR (AIRSAR) in Kojimawan, Japan, on October 4, 2000. They are in the L-band and covers 22 or 21 ships, as shown in Fig. 15(b) and (c) respectively. Further details on the dataset can be found in the literature [6] and at https://vertex.daac.asf.alaska.edu/. The analysis of the cross-polarization C-band data revealed that the sea state was moderate to high [6, 30]. Based on [30], the relationship between C-band cross-pol backscatter and wind speed is

$$\sigma^{o}_{cross-pol} = 0.592U_N^{10} - 35.6 \quad [dB] \tag{34}$$

where $\sigma^{o}_{cross-pol}$ is the cross-pol C-band scatter, and U_N^{10} is the equivalent neutral stability wind speed at a 10-m height above the ocean surface. The averaged wind speed in the AIRSAR dataset is estimated to be 12.5 m/s using the Vachon's method, signifying a moderate to high sea state. Here we choose two different areas B and C to assess the detection performances.

The first step in selecting some preliminary targets is to use a high threshold. Additionally, the clutter is selected using a low threshold, as when applying a truncated statistical model [31]. The ground truth is a key dataset in the assessment and generally it is hard to be obtained in practice. Therefore we choose two classical images where the ground truths have been accepted. It has been validated by visual inspection in previous studies [32] for AIRSAR dataset, which verify the true ships via combing the L-Band image and C-Band image. For the Radarset-2 dataset, the AIS aided to ensure the true ships. To be more accurate, we decrease the detection threshold to find enough ship pixels as the ground truth, which will not affect the performance assessment via the same assessment methods, although it may involve some edge pixels between ships and clutter.

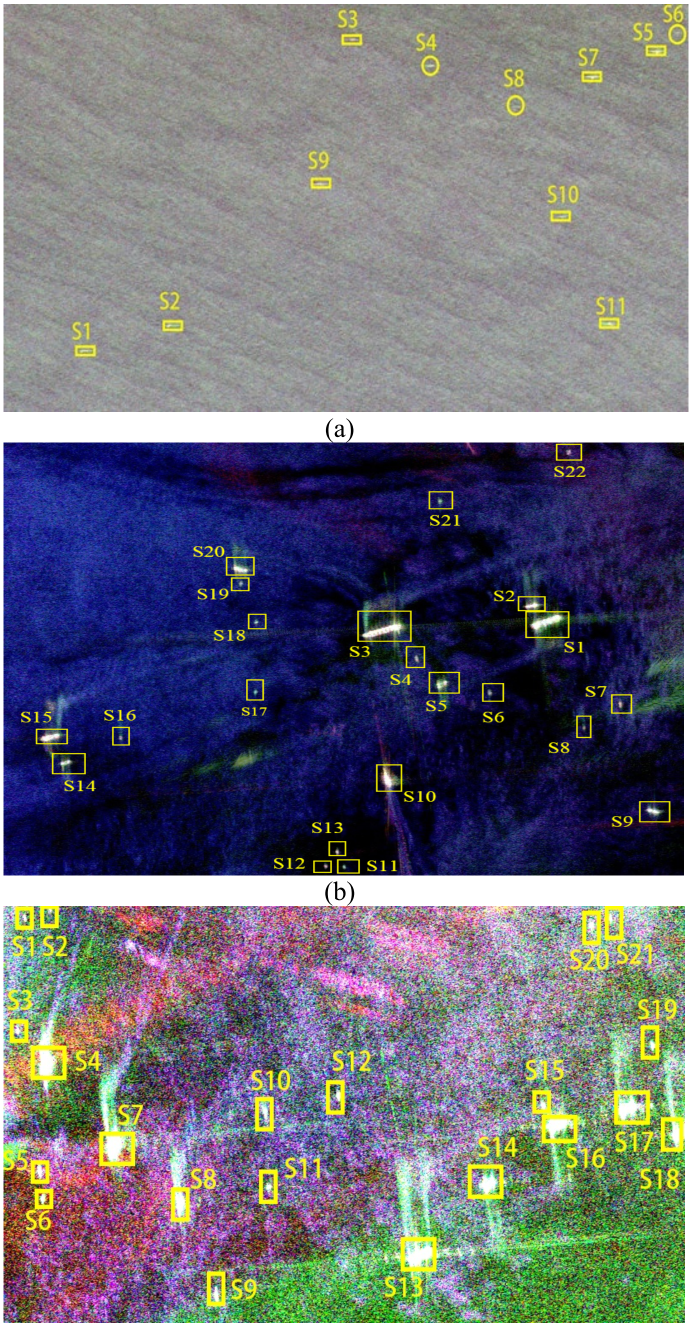

(a)

(b)

(c)

Fig. 15. The measured PolSAR images: (a) The selected RS-2 image : A (b) The selected AIRSAR image: B (c) The selected AIRSAR image: C

C. CFAR detection by the GΓD Model

The quadratic form of z=tr(**GC**) approximately obeys a gamma distribution $z \sim \gamma(\alpha, \beta)$ [6]. To deal with heavier tails and increase the accuracy of the CFAR, the GΓD can be used to model the output since the gamma distribution is a special case of the GΓD family for simplicity. The gamma distribution can be rewritten as

$$f(z;k,v,\sigma) = \frac{|v|k^k}{\sigma\Gamma(k)}\left(\frac{z}{\sigma}\right)^{kv-1}\exp\left\{-k\left(\frac{z}{\sigma}\right)^{v}\right\} \tag{34}$$

k, v, and σ are the shape, power, and scale parameters, respectively. In the GΓD case, the PFA can be rewritten as

$$P_{fa}=\int_{T}^{\infty} f(z;k,v,\sigma)dz=\begin{cases}1\text{-}\Gamma[k,\eta T^{v}], v>0\\ \Gamma[k,\eta T^{v}], v<0\end{cases} \tag{35}$$

and the threshold is

$$T=\begin{cases}\left(\dfrac{1}{\eta}\Gamma^{-1}[k,1\text{-}P_{fa}]\right)^{1/v}\\ \left(\dfrac{1}{\eta}\Gamma^{-1}[k,P_{fa}]\right)^{1/v}\end{cases} \tag{36}$$

where $\eta=k\sigma^{-v}$. The GΓD is employed as an extension to accommodate cases with heavier tails.

To build the higher dimensional space, we used the polarimetric and neighborhood covariance matrix using horizontal-vertical neighborhood collection in RADARSat-2 imagery. Because there is no polarimetric scattering matrix in the multilook format in the AIRSAR dataset, we only use the polarimetric covariance matrix itself without spatial information. The covariance matrices of ships and clutter are estimated using the maximum likelihood estimation (MLE) method. If the distribution of ships is dense, truncated statistics can be used for accurate estimation by removing large values [31].

D. *Performance Validation Indexes*

The CFAR loss is used to assess the statistical model fitness and is defined as in [29]:

$$C_L=\left|20\log\left(\overline{P}_{fa}\Big/\widehat{P}_{fa}\right)\right| \tag{37}$$

where C_L is a function dependent on the threshold and indicates the corresponding error between the actual PFA ($\overline{P}_{fa}$) and PFA ($\widehat{P}_{fa}$) estimated by the model.

Two factors are used to assess the detector performance over the measured data: (1) the ROC curves and the corresponding AUCs, and (2) the figure of merit (FOM). The FOM is a macroscopic index for performance evaluation and is based on the target number of detections in the final map [6]:

$$FoM=\frac{N_{td}}{\left(N_{fa}+N_{gt}\right)} \tag{38}$$

where N_{td} is the number of detected targets, N_{fa} is the number of false alarms, and N_{gt} is the total number of targets in the scene. The bisection search method is used to determine the adaptive threshold that can maintain the FA constant. Here, we assume that a ship pixel represents one target [6, 14, 33].

E. *Experiments by the measured datasets*

1) *Validation in North Sea Dataset*

The measured data were processed using different polarimetric detectors. The density-based clustering algorithm DBSCAN is applied to discover erring clusters in noisy images [6]. Here, we use a distance parameter ε equal to 100 and a point number *tol* equal to 8 in the DBSCAN algorithm to cluster the ship pixels. The detection result of SPDOF-9, which means the SPDOF detector with a dimension of 9, is presented in Fig. 16. × denotes the false alarm pixels. There were 12 targets in this study. It should be noted that only 11 ships had AIS certification. Because each effective detector found the twelfth ship, we assume it is the 12-th ship.

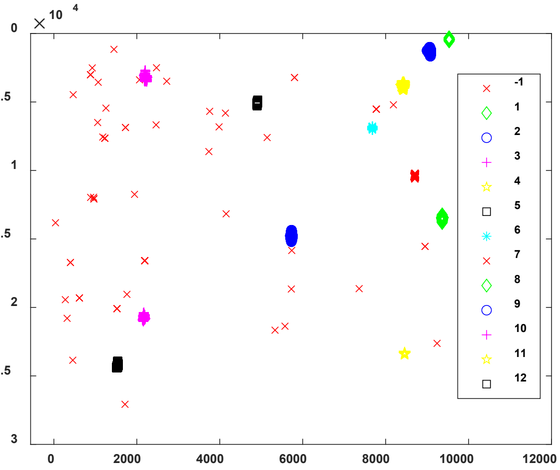

Fig. 16. Detection results of SPDOF-9.

Here, the CFAR is set to 1e-6. These quantities are listed in Table XII. Because C_L is not the same, the FOM cannot be used to compare the performances of different detectors. Moreover, the GΓD model cannot fit the statistics well. Finally, ROC curves were drawn based on the number of pixels of the target ship on the resulting graph.

TABLE XII
PERFORMANCE COMPARISON OF THE DIFFERENT DETECTORS. IN RS-2

Image	Method	N_{td}	N_{fa}	C_L	FoM(%)
RS-2	Joint-1	9412	68	11.41	94.46
	Joint-2	9412	68	11.41	94.46
	Joint-3	9412	68	11.41	94.46
	Joint-4	9419	69	11.53	94.52
	M-S	9423	70	11.66	94.55
	M-E	/	/	/	/
	M-A	9147	96	14.40	91.54
	S-E	9419	69	11.53	94.52
	S-A	9412	68	11.41	94.46
	E-A	8977	95	14.31	89.85
	SPDOF-9	9463	79	12.71	94.87
	APDOF-9	9896	99	14.67	99.01
	EVD-9	9210	67	11.28	92.44
	OPD	4882	128	16.90	48.70
	PWF	4672	178	19.76	46.38
	PNF	3019	45	7.82	30.37
	MCSR-9	7354	38	6.35	74.03
	DL(-5)	9479	82	13.03	95.00

It should be noted that M-E gives the worst performance, and too many false alarms make the clustering unable to work. Therefore, we use "/" to symbolize a very large number of FAs. In the following performance comparisons, the ROCs were presented to assess different polarimetric detectors.

The optimal dimensions of a single detector are shown in Fig. 17. The results are consistent with those of the numerical calculation and the simulated experiment. It can be seen that

MCSR-9 gives the best performance in the MCSR subspace detectors, and SPDOF 9-15 gives almost the same performance in the PDOF subspace detectors. The starting point of the abscissa is not consistent with the simulated data part because the pixel numbers are different, which should make the false alarm rate reasonable.

The joint detectors are shown in Fig. 18. All the joint detectors, including 1 to 4 dimensional subspaces combined by the MLDA method, provide almost the same high performance. Compared with the single polarimetric detector, SPDOF-9 provides the best performance, and it is very close to the joint detectors. In Fig. 18(b), the detection performances of the joint detectors combined with two simple detectors are presented and compared with those of the four detectors combinations. It can be seen that SPDOF-APDOF provides the best performance, which is even better than the joint detectors using four subspaces (Joint1-4). The EVD-APDOF clearly yielded the worst results.

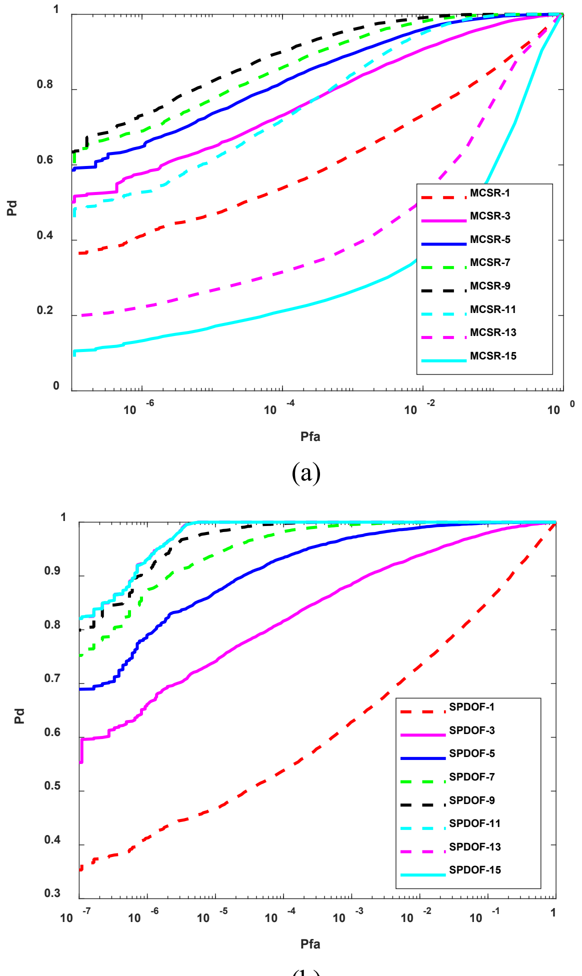

(a)

(b)

Fig. 17. ROCs of 1-15 dimensional subspaces in RS-2 imagery, (a) MCSR: 1-15 (b) PDOF: 1-15.

The detection performance of the DLDs with different factors is presented in Fig. 18. This is the same as the SPDOF when $\eta=0$. DLFs($\eta=0,-1,-5,-10$) are almost the same because the statistics of clutter and ships are Wishart models [6].

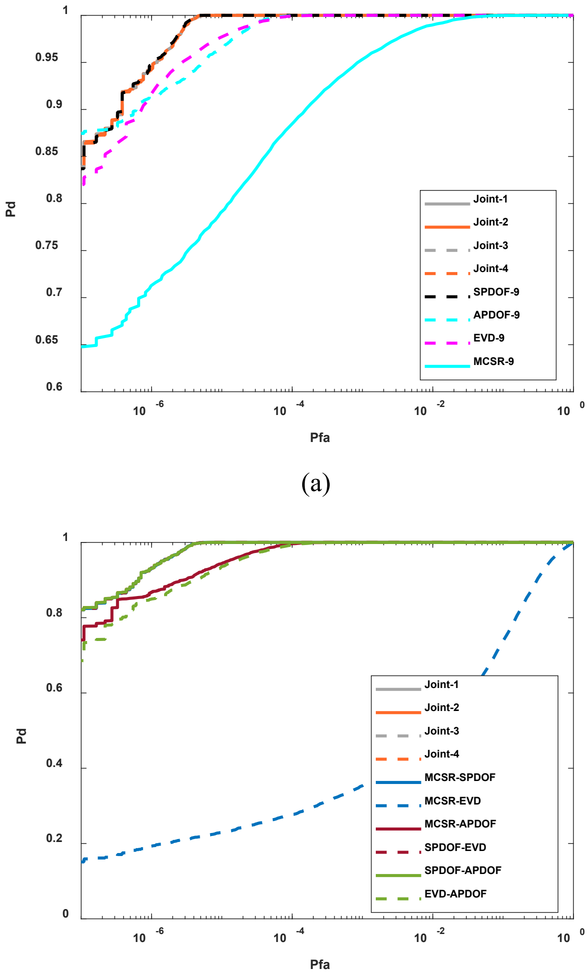

(a)

(b)

Fig. 18. ROCs of different joint subspaces detectors in RS-2. (a) Joint subspaces detector-4 subspaces(b) Joint subspace detector-2 subspaces

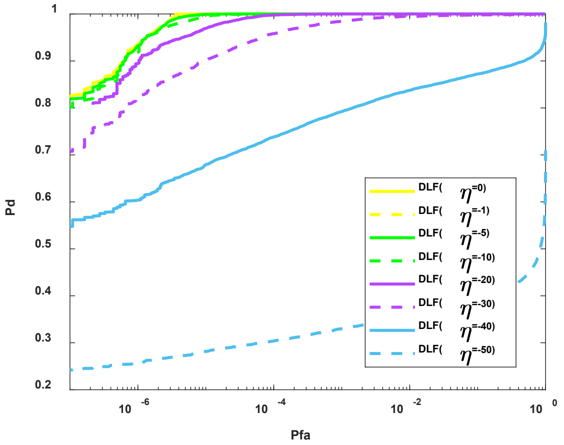

Fig. 19. The ROCs of DLDs with different DLFs in RS-2.

The comparisons among the classical polarimetric detectors, such as PWF, Reflection Symmetry (RS) [34], PNF, are presented in Fig. 20. It can be seen DLD gives the best performance and the RS would be the worst. The joint detectors are almost overlapped by the SPDOF-APDOF and DLD. It should be noted that the dimensions are all 3 instead of 15 for fair in the comparison simulation because OPD, RS and PNF are obtained in the 3-dimensional case.

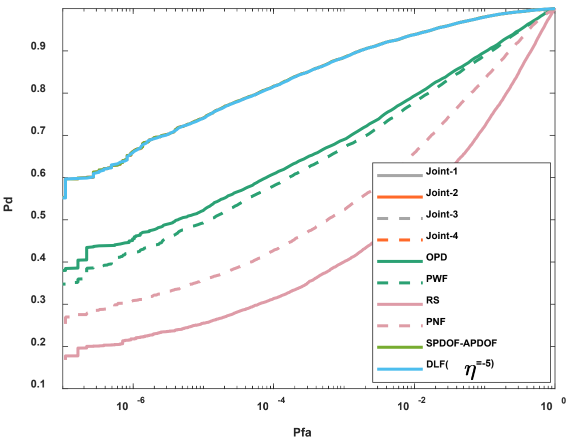

Fig. 20. ROC curves of traditional detectors in the RS-2 image.

2) Validation in AIRSAR Dataset

In the AIRSAR imagery, the data format is a multilook complex (MLC); therefore, the full dimension is 3, and the neighborhood information is not used in our experiments. The parameters of MLDA are still in the normal state, except β=1e6, owing to the large TCR. The pixel-based FOM and ROC curves were used for evaluation.

In the area B, the result of Joint-3 is shown in Fig. 21 as an example. There are 23 targets in the scene, instead of 22. Ship wakes from a ship are seen as targets here because this is also a feature of one ship and can be seen as weak targets. Of course, if wakes are not seen as targets, the results of performance comparisons will not change, but Pfa will increase.

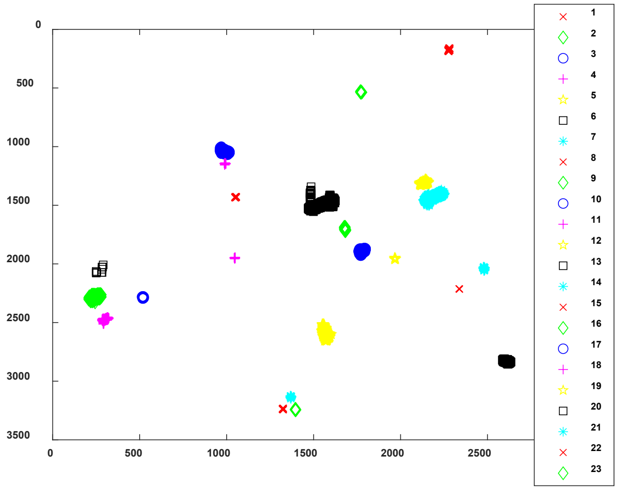

Fig. 21. Detection Results of the Joint-3 detector in AIRSAR B.

Here, the CFAR is set to 1e-5. The values of different polarimetric detectors are listed in Table XIII, where the N_{fa} of each detector is zero. This is caused by the high threshold. We can see that the clutter background is very complicated, and the statistical GΓD model cannot fit the measured data effectively. In addition, the FOM cannot be used to assess the detection performance because the actual false alarm rate is not constant.

TABLE XIII
PERFORMANCE COMPARISON OF THE DIFFERENT DETECTORS IN AIRSAR IMAGERY B

Image	Method	N_{td}	N_{fa}	C_L	FoM(%)
AIR SAR B	Joint-1	2123	0	/	94.48
	Joint-2	2123	0	/	94.48
	Joint-3	2123	0	/	94.48
	Joint-4	2123	0	/	94.48
	M-S	2123	0	/	94.48
	M-E	1118	0	/	49.76
	M-A	2146	0	/	95.51
	S-E	2123	0	/	94.48
	S-A	2123	0	/	94.48
	E-A	2146	0	/	95.51
	SPDOF-2	2117	0	/	94.21
	APDOF-2	2153	0	/	95.82
	EVD-2	2124	0	/	94.53
	OPD	2155	0	/	95.91
	PWF	2150	0	/	95.68
	PNF	1821	3	/	81.04
	MCSR-2	2089	0	/	92.97
	DL(770)	2247	0	/	100.00

All the ROC curves of the different polarimetric detectors are presented in Fig. 22-23. Fig. 22(a) shows the performances of single detectors with different dimensional subspaces. We found that EVD-2 gave the best performance, followed by SPDOF-2. Fig. 22 (b) also shows that EVD-2 provides the best performance compared with the Joint1-4 detectors.

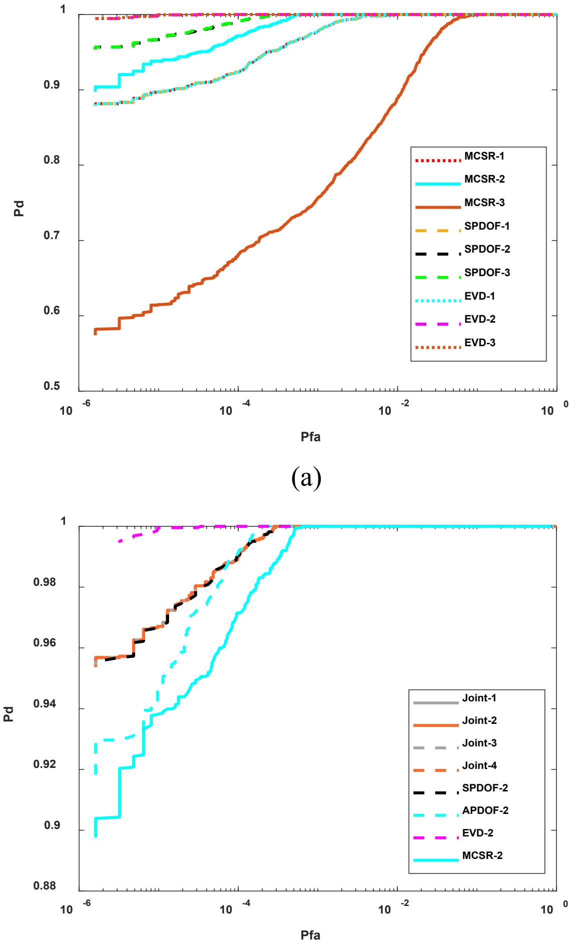

(a)

(b)

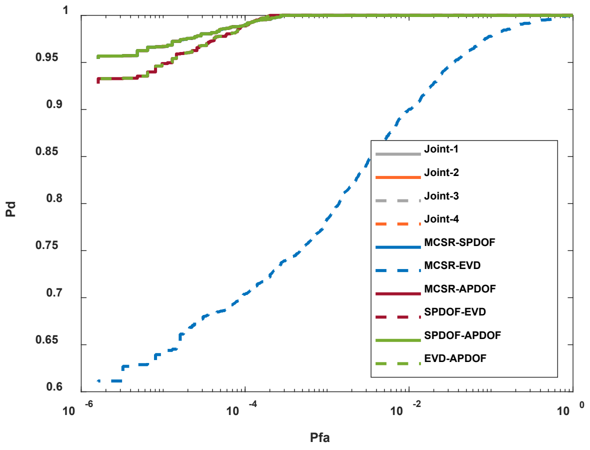

(c)

Fig. 22. ROCs of different detectors in the AIRSAR image B. (a) Single detectors with different subspace dimension (b) Joint subspaces detector-4 subspaces (c) Joint subspace detector-2 subspaces.

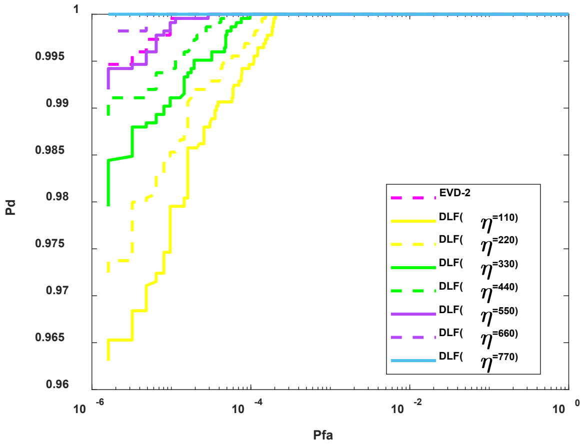

Fig. 23. ROC curves of DLDs in the AIRSAR image B.

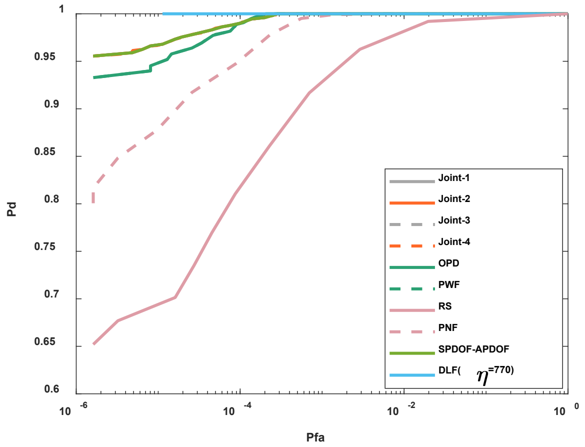

Fig. 24. ROC curves of traditional detectors in the AIRSAR image B.

In theory, EVD is an approximate solution of GEVD, and GEVD is the same as APDOF. Therefore, the EVD should be close to APDOF. Here, we believe the fact that EVD-2 provides the best performance is coincidental. This assumption is verified by changing the region of clutter. Additionally, we used the DLD method to find a better detector than EVD. The results are presented in Fig. 23. This shows that the DLD with a suitable diagonal loading factor always achieves the best detection performance.

The detection results between different classical polarimetric detectors are similar to RS-2's, which are presented in Fig. 24. DLD gives the best performance and the RS would be the worst. The OPD is overlapped by the PWF. The joint detectors are almost overlapped by the SPDOF-APDOF.

In the area C, the detection result of PWF is shown in Fig. 25 as an example. We can see that there are 23 targets in the scene, instead of 21. One is a false alarm, and the other is ship wake. Ship wake from a ship can be seen as a target since it helps to find the small ships. The FOM is listed in Table XIV. The CFAR is set as 1e-5. The results are almost the same as that in Table XIII.

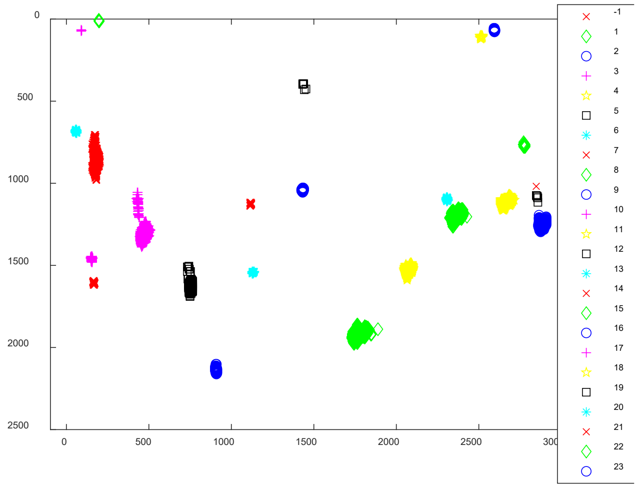

Fig. 25. Detection Results of the PWF detector in AIRSAR image C

TABLE XIV
PERFORMANCE COMPARISON OF THE DIFFERENT DETECTORS IN AIRSAR IMAGERY C

Image	Method	N_{td}	N_{fa}	C_L	*FoM*（%）
AIR SAR C	Joint-1	1873	0	/	71.22
	Joint-2	1873	0	/	71.22
	Joint-3	1873	0	/	71.22
	Joint-4	1873	0	/	71.22
	M-S	1873	0	/	71.22
	M-E	2026	4	/	77.03
	M-A	1992	2	/	75.74
	S-E	1873	0	/	71.22
	S-A	1873	0	/	71.22
	E-A	1992	2	/	75.68
	SPDOF-2	1923	2	/	73.06
	APDOF-2	1911	1	/	72.63
	EVD-2	1904	1	/	72.37
	OPD	1991	2	/	75.65
	PWF	1992	2	/	75.68
	PNF	2182	6	/	82.78
	MCSR-2	1786	3	/	67.83
	DL(1e5)	2630	7	/	99.73

All the ROCs of the different polarimetric detectors in area C are presented in Fig. 26 and 27. We can find the 2-dimensional and 3-dimensional subspace detectors have almost the same performances in Fig. 25(a). The results are consistent with those in area A and area B. Here the PWF reaches the best performance, which can be seen as a special case of the DLD.

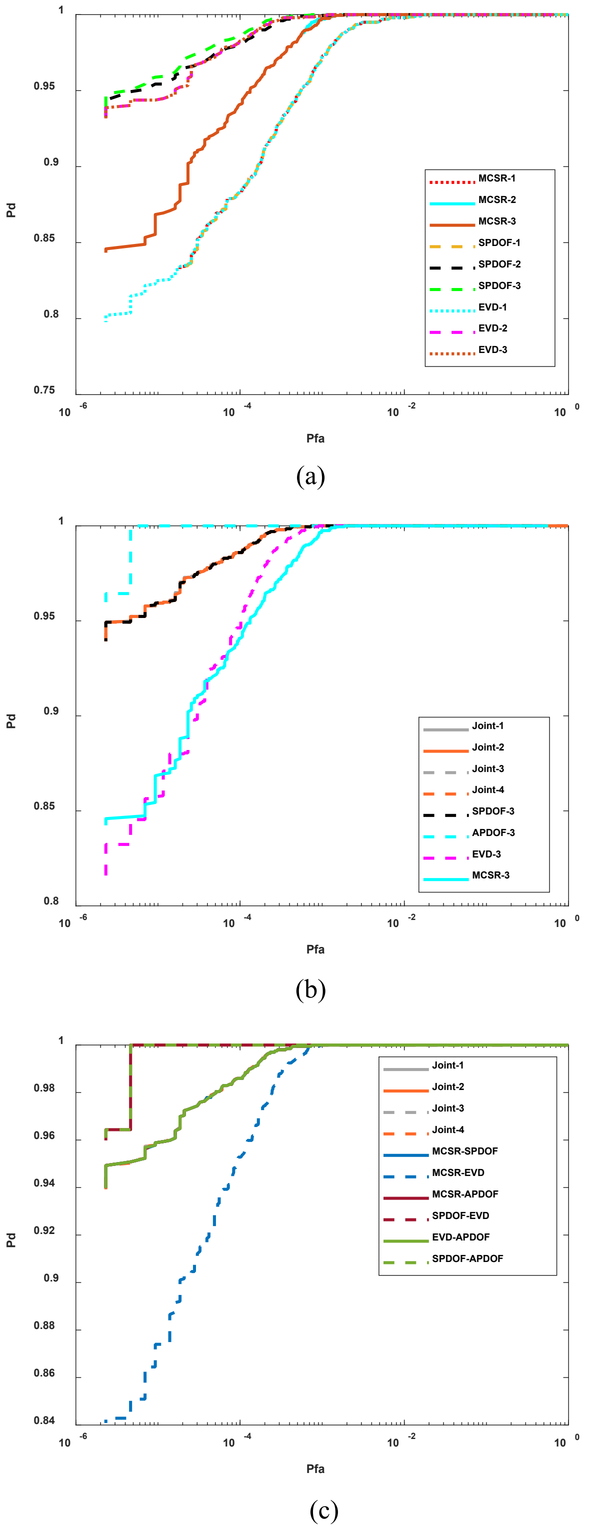

(a)

(b)

(c)

Fig. 26. ROCs of different detectors in the AIRSAR image C. (a) Single detectors with different subspace dimension (b) Joint subspaces detector-4 subspaces (c) Joint subspace detector-2 subspaces.

In Fig. 27, the performances of the DLD detectors with different DLF are presented. It can be seen that the larger the DLF is, the better the performance would be. This also shows that the PWF should reach the best performance in the DLDs as a special case.

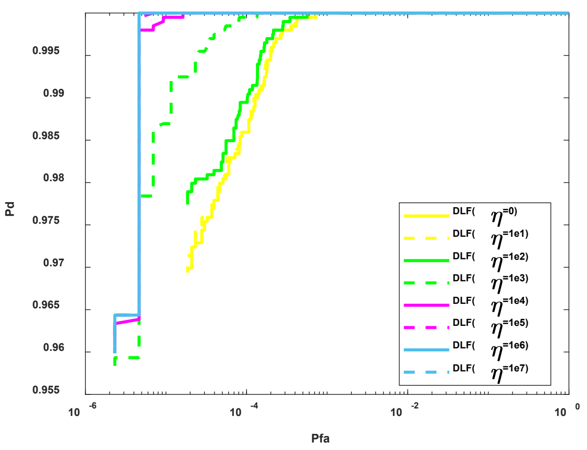

Fig. 27. ROC curves of DLDs in the AIRSAR image C.

The comparisons between the classical polarimetric detectors, such as PWF, RS, PNF, are presented in Fig. 28. It can also be seen DLF gives the best performance and the RS would be the worst. The OPD is overlapped by the PWF. The joint detectors are almost overlapped by the SPDOF-APDOF.

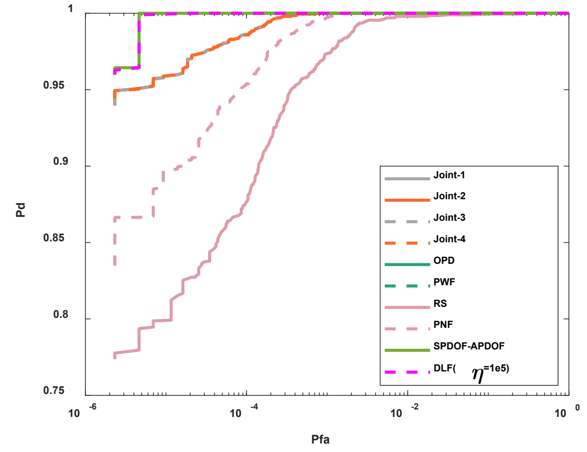

Fig. 28. ROC curves of traditional detectors in the AIRSAR image C

V. CONCLUSION

This study focused on PolSAR ship detection. First, the APDOF was improved to a strict formalism—SPDOF, which included the full-dimensional case of PDOF, while the approximate one did not. The SPDOF transformed the PolSAR image into a subspace in which the ratio of TCR and clutter fluctuation reached the maximum, showing the best detection ability in single polarimetric detectors, regardless of the Wishart background or complex clutter environment.

Then, a joint detector was proposed based on the MLDA method, which showed strong robustness and detection capabilities. It combined different detectors to maximize the detection efficiency, in contrast to a single detector, which is only suited for one optimization objective function.

The best performance of the joint mainly comes from the combination of two detectors, SPDOF and APDOF. To further improve the detection ability, the linear coefficient provided by the MLDA theory was used as the initial value, and the eigenvalue was used to optimize the proportion of SPDOF and APDOF. Finally, SAPDOF, which can achieve the best detection under various environments, was proposed, providing a strong practical application for PolSAR ship detection.

In addition, the main line of work detailed above, this paper presents an efficient and simple numerical operation method to determine the optimal dimensions of the subspace detector. The accuracy of this method was verified by simulation and real data. At the same time, the relationship between MCSR, EVD, and APDOF detectors, which involve trace ratio and ratio trace problems, was also clarified in this study. The GEVD was proven to be the same as the APDOF.

There are many ship detection approaches based on the deep learning at present. To our best knowledge, the open PolSAR benchmark dataset are very few and the deep learning is data-driven and data-sensitive. In our future work, we will aim to step into interpretable deep learning, hoping to conduct a more in-depth analysis of small ships detection, including ship wakes detection, by finding novel neural networks and trying to explain their physical meaning.

VI. REFERENCES

[1] D. Crisp, "The state-of-the-art in ship detection in Synthetic Aperture Radar imagery," DSTO, Department of Defence, Canberra, ACT, Australia, vols. 05/01, 2004.

[2] G. Gao and G. Shi, "CFAR ship detection in nonhomogeneous sea clutter using polarimetric SAR data based on the notch filter," in *IEEE Trans. Geosci. Remote Sens.*, vol. 55, no. 8, pp. 4811–4824, Aug. 2017. doi: 10.1109/TGRS.2017.2701813.

[3] K. Ouchi, "Current status on vessel detection and classification by synthetic aperture radar for maritime security and safety," in *Proc. Symp., Remote Sens. Environ.* Aichi, Japan: Sci, pp. 5–12, Sep. 2016.

[4] C. Brekke and S. N. Anfinsen, "Ship detection in ice-infested waters based on dual-polarization SAR imagery," in *IEEE Geosci. Remote Sens. Lett.*, vol. 8, no. 3, pp. 391–395, May 2011. doi: 10.1109/LGRS.2010.2078796.

[5] M. Sciotti, D. Pastina, and P. Lombardo, "Polarimetric detectors of extended targets for ship detection in SAR images," in *Geoscience and Remote Sensing Symposium*. Sydney, NSW, Australia, Australia, Jul. 2001.

[6] T. Liu, Y. Jiang, A. Marino, G. Gao, and J. Yang, "The polarimetric detection optimization filter and its statistical test for ship detection," in *IEEE Trans. Geosci. Remote Sens.,* vol. PP, vol. 99, pp. 1–18, 2021.

[7] T. Liu, Z. Yang, T. Zhang, Y. Du, and A. Marino, "A new form of the polarimetric notch filter," in *IEEE Geosci. Remote Sensing Lett.*, vol. 99, pp. 1–5, 2020. doi: 10.1109/LGRS.2020.3020052.

[8] F. Biondi, "A polarimetric extension of low-rank plus sparse decomposition and radon transform for ship wake detection in synthetic aperture radar images," in *IEEE Geosci. Remote Sens. Lett.*, vol. 16, no. 1, pp. 75–79, 2019. doi: 10.1109/LGRS.2018.2868365.

[9] K. Jin, Y. Chen, B. Xu, J. Yin, X. Wang, and J. Yang, "A patch-to-pixel convolutional neural network for small ship detection with PolSAR images," in *IEEE Trans. Geoence Remote Sens.*, vol. 99, pp. 1–16, 2020. doi: 10.1109/TGRS.2020.2978268.

[10] L. M. Novak, M. B. Sechtin, and M. J. Cardullo, "Studies of target detection algorithms that use polarimetric radar data," in *IEEE Trans. Aerosp. Electron. Syst.,* vol. 25, no. 2, pp. 150–165, 1989. doi: 10.1109/7.18677.

[11] A. B. Kostinski and W. M. Boerner, "On the polarimetric contrast optimization," in *IEEE Trans. Antennas Propag.,* vol. 35, no. 8, pp. 988–991, 1987. doi: 10.1109/TAP.1987.1144209.

[12] W. M. Boerner, and A. B. Kostinski, "On the concept of the polarimetric matched filter in high resolution radar imaging: An alternative for speckle reduction," in *Antennas and Propagation Society International Symposium*, pp. 69–72, 1988.

[13] J. Yang, G. Dong, Y. Peng, Y. Yamaguchi, and H. Yamada, "Generalized optimization of polarimetric contrast enhancement," in *IEEE Geosci. Remote Sens. Lett.,* vol. 1, no. 3, pp. 171–174, 2004. doi: 10.1109/LGRS.2004.830127.

[14] D. Yang, L. Du, H. Liu, and W. Ni, "Novel polarimetric contrast enhancement method based on minimal clutter to signal ratio subspace," in *IEEE Trans. Geosci. Remote Sens.,* vol. 57, no. 11, pp. 8570–8583, 2019. doi: 10.1109/TGRS.2019.2921629.

[15] R. Touzi, J. Hurley, and P. W. Vachon, "Optimization of the degree of polarization for enhanced ship detection using polarimetric RADARSAT-2," in *IEEE Trans. Geosci. Remote Sens.*, vol. 53, no. 10, pp. 5403–5424, Oct. 2015. doi: 10.1109/TGRS.2015.2422134.

[16] R. Touzi, F. J. Charbonneau, R. K. Hawkins, and P. W. Vachon, "Ship detection and characterization using polarimetric SAR," in *Can. J. Remote Sens.*, vol. 30, no. 3, pp. 552–559, 2004. doi: 10.5589/m04-002.

[17] L. M. Novak and M. C. Burl, "Optimal speckle reduction in polarimetric SAR imagery," in *IEEE Trans. Aerosp. Electron. Syst.*, vol. 26, no. 2, pp. 293–305, 1990. doi: 10.1109/7.53442.

[18] A. Marino, "A notch filter for ship detection with polarimetric SAR data," in *IEEE J. Sel. Top. Appl. Earth Obs. Remote Sensing*, vol. 6, no. 3, pp. 1219–1232. doi: 10.1109/JSTARS.2013.2247741.

[19] L. M. Novak, "Target detection studies using fully polarimetric data collected by the Lincoln Laboratory MMW SAR," *92 Intl. Conf. on Radar*, Brighton, UK, pp. 167–170, 1992.

[20] R. Zhang, F. Nie, X. Li, and X. Wei, "Feature selection with multi-view data: A survey," in *Inf. Fusion*, vol. 50, pp. 158–167, 2019. doi: 10.1016/j.inffus.2018.11.019.

[21] J. Yin, J. Yang, C. Xie, Q. Zhang, Y. Li, and Y. Qi, "An improved generalized optimization of polarimetric contrast enhancement and its application to ship detection," in *IEICE Trans. Commun.*, vol. E96b, no. 7, pp. 2005–2013, 2013.

[22] T. Liu, "Comments on novel polarimetric contrast enhancement method based on minimal clutter to signal ratio subspace," in *IEEE Transactions on Geoscience and Remote Sensing*, 1–2. doi: 10.1109/TGRS.2021.3087138.

[23] H. Wang, S. Yan, D. Xu, X. Tang and T. huang, "Trace Ratio vs. ratio Trace for Dimensionality Reduction," in *IEEE Conf. on Comput. Vis. and Pattern Recognit.*, Minneapolis, MN, USA, pp. 1–8, 2007. doi: 10.1109/CVPR.2007.382983.

[24] M. Zhao, Z. Zhang, T. Chow,"Trace ratio criterion based generalized discriminative learning for semi-supervised dimensionality reduction," in *Pattern Recognit.*, vol. 45, no. 4, pp. 1482–1499, Apr. 2012. doi: 10.1016/j.patcog.2011.10.008.

[25] D. Li and Y. Zhang, "Random similarity Between two mixed scatterers," in *Geosci. Remote Sens. Lett. IEEE,* vol. 12, no. 12, pp. 2468–2472, 2015.

[26] C. Forbes *et al.*, *Statistical Distributions*, 4th ed. Hoboken, NJ, USA: Wiley, 2010.

[27] M. Zhao, M. Lin, B. Chiu, Z. Zhang and X. Tang, "Trace Ratio Criterion based Discriminative Feature Selection via L2,p-norm regularization for supervised learning," in *Neurocomputing*, vol. 321, pp. 1–16, 2018. doi: 10.1016/j.neucom.2018.08.040.

[28] T. Liu, Z. Yang, A. Marino, G. Gao and J. Yang, "PolSAR ship detection based on neighborhood polarimetric covariance matrix," in *IEEE Trans. Geosci. Remote Sens.*, vol. 59, no. 6, pp. 4874–4887, 2020. doi: 10.1109/TGRS.2020.3022181.

[29] T. Liu, J. Zhang, G. Gao and A. Marino, "CFAR ship detection in polarimetric synthetic aperture radar images based on whitening filter," in *IEEE Trans. Geosci. Remote Sens.*, vol. 58, no. 1, pp. 58–81, Jan. 2020. doi: 10.1109/TGRS.2019.2931353.

[30] P. W. Vachon and J. Wolfe, "C-band cross-polarization wind speed retrieval," in *IEEE Geosci. Remote Sens. Lett.*, vol. 8, no. 3, pp. 456–459, May 2011. doi: 10.1109/LGRS.2010.2085417.

[31] T. Liu, Z. Yang, A. Marino, G. Gao and J. Yang, "Robust CFAR detector based on truncated statistics for polarimetric synthetic aperture radar," in *IEEE Trans. Geosci. Remote Sens.*, vol. 58, no. 9, pp. 6731–6747, Sept. 2020. doi: 10.1109/TGRS.2020.2979252.

[32] J. Wei, P. Li, Y. Jie, J. Zhang and F. Lang, "A new automatic ship detection method using L-band polarimetric SAR imagery," in *IEEE J. Sel. Top. Appl. Earth Obs. Remote Sensing*, vol. 7, no. 4, pp. 1383–1393, 2014. doi: 10.1109/JSTARS.2013.2269996.

[33] T. Zhang, L. Jiang, D. Xiang, Y. Ban, L. Pei, and H. Xiong, "Ship detection from PolSAR imagery using the ambiguity removal

polarimetric notch filter," in *ISPRS Journal of Photogrammetry & Remote Sensing*, vol.157, pp. 41-58, 2019.

[34] E. Ferrentino, F. Nunziata, A. Marino, M. Migliaccio and X. Li, "Detection of wind turbines in intertidal areas using SAR polarimetry," in *IEEE Geosci. Remote Sens. Lett.*, vol. 16, no. 10, pp. 1516-1520, 2019.

Tao Liu received the B.S. degree in communication engineering and the Ph.D. degree in information and communication engineering, all from the National University of Defense Technology (NUDT), Changsha, China, in 2001 and 2007 respectively. Since 2007, he has been with the School of Electronic Engineering, Naval University of Engineering, where he is currently a Professor. He has authored over 50 journal papers and three books. His research interests include statistical theory of radar polarization, polarization information processing, synthetic aperture radar (SAR) automatic target recognition, statistical modeling of SAR image, SAR ship detection, InSAR (interferometric SAR), SAR ground moving target indication and Artificial Intelligence(AI).

Ziyuan Yang received the B.S. degree in radar engineering from the Naval University of Engineering (NUE), Wuhan, China, in 2019 .Now he is studying for a doctor's degree in information and communication engineering.

His research interests include radar polarization information process and electronic warfare system modeling and SAR ground moving target indication.

Armando Marino (M'2011) received the M.Sc. degree in telecommunication engineering from the Universita' di Napoli "Federico II," Naples, Italy, in 2006. In 2006, he joined the High Frequency and Radar Systems Department, German Aerospace Centre, Oberpfaffenhofen, Germany, where he developed his M.Sc. thesis. He received the Ph.D. degree in polarimetric SAR interferometry from the School of Geosciences, University of Edinburgh, Edinburgh, U.K., in 2011. From March 2011 to October 2011, he was with the University of Alicante, Institute of Computing Research, Spain. From December 2011 to May 2015, he was a Postdoctoral Researcher and Lecturer with ETH Zurich, Institute of Environmental Engineering, Switzerland. From June 2015, he was a Lecturer with the School of Engineering and Innovation, Open University, Milton Keynes, U.K. Since May 2018 he is a Senior Lecturer (Associate Professor) at the University of Stirling, Faculty of Natural Sciences, Stirling, UK.

Gui Gao (M'09) received the B.S. in information engineering, the M.S. and Ph.D. degrees in remote sensing information processing from National University of Defense Technology (NUDT), Changsha, China, in 2002, 2003 and 2007, respectively.

From 2007, he joined the Faculty of Information Engineering, School of Electronic Science and Engineering, NUDT, as an associate professor. From 2017, he was with Faculty of Geosciences and Environmental Engineering, Southwest Jiaotong University, Chengdu, China, where he is currently a professor. He has authored over 100 journal and conference papers and has written four books and an English chapter. His current research interests include radar signal processing, InSAR (interferometric SAR), target detection, marine environment, and SAR GMTI (ground moving target indication).

Jian Yang (M'03, SM' 04) received the B.S. and M.S. degrees from Northwestern Polytechnical University, Xian, China, in 1985 and 1990, respectively, and the Ph.D. degree from Niigata University, Niigata, Japan, in 1999. In 1985, he joined the Department of Applied Mathematics, Northwestern Polytechnical University. From 1999 to 2000, he was an Assistant Professor with Niigata University. In April 2000, he joined the Department of Electronic Engineering, Tsinghua University, Beijing, China, and he was promoted to a full Professor in 2002. He has published more than 300 papers and received many awards. His research interesting areas include radar polarimetry, feature extraction, target detection and target classification.